LU TP 19-...
June 2019

Patterning of the neural tube: A 3D computational modelling approach

Ariane Ernst

Department of Astronomy and Theoretical Physics, Lund University

Master thesis supervised by Dr. Victor Olariu

LUND
UNIVERSITY

Abstract

Neurodegenerative diseases such as Parkinson's can be treated with stem-cell derived specialized neurons. In order to achieve precise directed neural differentiation *in vitro* we need to understand the gene regulatory mechanisms behind *in vivo* neural tube patterning. We implement a 3D computational model of brain patterning to simulate this process. The mathematical model is set up by unifying two existing gene regulatory network models for patterning of the dorsoventral and rostrocaudal axes on the basis of WNT-signaling. A custom Python-based simulation tool was implemented in order to accurately simulate reaction-diffusion equations and signaling secretion sources. We discuss the validity of the implemented model and explore its properties in two different geometries. We find a possible correlation between dorsoventral patterning and vesicle formation as well as a segment in which fore-, mid- and hindbrain expression are stacked dorsoventrally. Furthermore, we identify a need for an adaption of one of the networks to signal exposure time. While it is hard to make any specific predictions for *in vitro* differentiation at this point, we have created a working fundament for future insights using our simulation tool and a more extensive mathematical model.

Popular Science Summary

In this work we simulate an important process of early embryonic neural development in three dimensions using gene regulatory networks (GRN). A GRN describes the interaction of chemical switches that keep a cell in its state or make it specialize to a specific type, e.g. neurons, using differential equations. Our aim is to make predictions on how we can direct neural cell specialization in the lab based on this model and the simulation tool we developed. These specialized cells can be used in various medical applications, for example to treat neurodegenerative diseases like Parkinson's. Computational and mathematical modelling and simulation comes with the advantage of reduced cost in comparison to experiments and it also allows us to understand the logic behind biological activities. The latter would not be possible without computational aid, since such processes often involve millions of molecules and even more complicated interactions. In this project we implement a 3D simulation program that models the GRN involved in early neural tube formation.

Populärwissenschaftliche Zusammenfassung

In dieser Arbeit simulieren wir einen wichtigen Prozess der frühen neuralen Embryonalentwicklung in drei Dimensionen mithilfe von genregulierenden Netzwerken (GRN). Ein GRN beschreibt die Wechselwirkung zwischen chemikalischen Schaltern, welche die Zelle in ihrem Zustand halten oder sie zu einer Spezialisierung, z.B. zum Neuron, veranlassen, unter Nutzung von Differentialgleichungen. Unsere Hoffnung ist, dass mithilfe des von uns entwickelten Modells sowie des Simulations-Tools in Zukunft Vorhersagen darüber getroffen werden können, unter welchen Bedingungen Zellen sich im Labor zur neuralen Spezialisierung veranlassen könnten. Solch spezialisierte Zellen können in verschiedenen medizinischen Gebieten Anwendung finden, z.B. um neurodegenerative Krankheiten wie Parkinson zu behandeln. Numerisches und mathematisches Modellieren und Simulieren hat einen deutlichen wirtschaftlichen Vorteil im Vergleich zur Laborarbeit und erlaubt uns außerdem, die biologischen Prozessen zugrunde liegende Logik zu verstehen. Letzteres wäre ohne die Hilfe eines Computers nicht möglich, da solche Vorgänge oft Millionen von Molekülen und noch mehr komplizierte Interaktionen involvieren. In diesem Projekt implementieren wir ein 3D Simulations-Programm, welches die an der frühen Formation des Neuralrohrs beteiligten GRN modelliert.

Contents

1 Introduction

> "What is found in biology is *mechanisms*,
> mechanisms built with chemical components and that are often modified by other, later, mechanisms added to the earlier ones."
>
> —Francis Crick

Of all the cell types found in the human body, neurons display the greatest diversity of structures, function and genetic makeup [1]. In fact, the multitude of neural variants just in the brain is so vast that biologists are still struggling to devise an adequate classification system [2]. Unfortunately, it is with this incredible variety that science is also faced with a great amount of devastating neurological disorders and illnesses, such as Alzheimer's disease, multiple sclerosis or Parkinson's disease; many of which were deemed incurable for a long time [3]. In 1981, the first identification and successful culture of mouse embryonic stem cells offered a new solution [4]. Stem cells are self-renewing cells that can give rise to any other type of cell in the body [5]. This makes them incredibly well suited as candidates for a treatment of neurological, especially neurodegenerative, disorders: a transplantation of new, healthy neurons generated *in vitro*, possibly even from the patient's own stem cells, could replace what was lost to the illness.
Today, almost 40 years later, several research groups have indeed successfully achieved partial recovery e.g. in parkinsonian monkeys and rats using exactly this method [6] [7]. There are however still some obstacles preventing us from safely translating the procedure from animal models to clinical application. One of the main issues is the reliable specialization, or *differentiation*, of stem cells into the required cell type. For example, in Parkinson's disease, the dopamine-producing (*dopaminergic*) neurons from the substantia nigra of the brain undergo pathological deterioration. A successful therapy approach would therefore entail directed differentiation of stem cells into dopaminergic neurons. While experimental protocols to this end have been implemented already [8], they still suffer from issues such as sample impurity [9]. This is because the complicated underlying epigenetic processes of neural differentiation are not yet fully known – only when we really understand the mechanisms that we find *in vivo* will we be able to accurately implement and modify them.

This thesis aims to improve our understanding of one of the very early, but very important cell specification activities: the early patterning of the anterior human neural tube into different brain cell progenitors. The neural tube is - as the name suggests - a tubular structure that forms around three weeks post fertilization in the vertebrate

embryo [5]. Cells at the head end of the tube are responsible for giving rise to all types of brain cells during further development – including e.g. the aforementioned dopaminergic neurons. In order to control this complex but nonetheless self-organizing process from early on, cells are predisposed towards their respective developmental paths. This predisposition is mainly controlled by cell position, which is why we subdivide the brain into fore-, mid- and hindbrain. For example, cells that acquire forebrain progenitor identity will not give rise to dopaminergic neurons, but midbrain progenitor cells will [8]. Progenitor character does not necessarily have to show under a microscope as a change of structure of the cell, but can just mean the expression of certain genes.

Figure 1: Human embryo at 24 days (dorsal view), clearly showing the neural tube along the length of body [10].

This process of predisposition according to location is what we call *patterning*. Since cells have no direct way to 'see' their positional information, nature often utilizes the release of protein signals from some source. Such a signal can diffuse through the tissue and thereby form a concentration gradient. Within each cell, a system regulating genetic expression and thus protein synthesis then reacts according to the signal concentration, and patterning is achieved [5].

The exact mechanisms of genetic regulation and signaling involve millions of molecules and are thus impossible to comprehend on that level of detail. We can however model the underlying logical circuits using ordinary differential equations. In this project we will combine two previously suggested models of gene expression along different axes of the neural tube and simulate the resulting patterning in three dimensions.

Our main objective is to build a model that makes accurate predictions on the differentiation behaviour of neural tube cells and hence helps us find new experimental protocols for that purpose, e.g. in order to be able to cultivate purer dopaminergic neuron transplants. To that end, we need to find a connecting element between existing models and explore how the simulated behaviour of the unified system compares to *in vivo* observations.

The second main goal of the project is the development of a computational tool to simulate the processes described above. This program needs to be able to take three-dimensional shapes as well as specific secretion locations as input and numerically solve

reaction-diffusion equations within these boundaries. In the future, this could possibly be applied to many of the various different patterning processes found in biology [5].

In the course of this thesis, we will at first give a more detailed introduction to the biological background and the two models used in section 2. The main results, including the simulation tool, the unified model and simulations with two different geometries, are discussed in section 3 and a conclusion is given in chapter 4. We will then explain the computational and physical methods used in the simulation in chapter 5. Some acknowledgements can be found in section 6. Finally, additional information as well as supplementary figures can be found in appendix 7.

2 Background

One of the greatest wonders of biology is how entire organisms can emerge from just the combination of a sperm and an egg. The sheer complexity of the human body shows us that this must require a great amount of organization and structuring even from the earliest stages of embryonic development on. The cellular system that we model in this thesis, the *neural tube*, is an important part of the vertebrate embryo and responsible for the formation of the central nervous system (CNS). To achieve the best understanding of the involved biophysical processes, we are going to outline the very early stages of in vivo human prenatal development with emphasis on neural tube formation. All developmental stages will be specified by an approximate number of days (d) after conception (which might vary between embryos) according to [11], [12] and [13]. Nomenclature guidelines from [14] are followed - gene symbols will be written in italic (*Shh*), protein symbols are non-italicized (Shh) and symbols will be in uppercase if they are human-specific (e.g. *SHH* or SHH).

2.1 Early Human Embryogenesis and Neural Tube Formation

From the egg to the neural tube

In order to understand the process of neural tube formation one has to begin by exploring early human embryogenesis, which begins with fertilization (0d) and ends with the formation of the neural tube (26d).

17 days after fertilization, following days of cleavage and implantation, the embryo undergoes a major change: the formation of the three germ layers, also called *gastrulation*. During this process, the embryonic disk divides into three layers (*ectoderm*,*endoderm*,*mesoderm*) responsible for giving rise to different types of tissue during further development. The top layer, the *ectoderm*, is responsible for the formation of skin and the central as well as peripheral nervous system and thus of most relevance for this thesis [5].

After germ layer formation, the *neural plate* is formed during a process called *neural induction* (18d, see Figure 2). The neural plate appears as a kind of thickened oval part of the ectoderm and consists of a morphologically homogeneous sheet of epithelial cells. On around the 20th day, *neurulation* begins: a furrow – the *neural groove* – appears on the neural plate and starts to deepen, while the surrounding neural plate tissue folds upwards until the left and right side meet to form a hollow tube which we call the *neural tube* [15]. (In the human embryo, this complicated, failure-prone closure process happens at different times for different locations and takes up until day 28. Closure

defects can lead to serious conditions such as spina bifida.) On a cellular level, the cells change from a cuboidal shape to elongated, pseudostratified neuroepithelial cells [5].

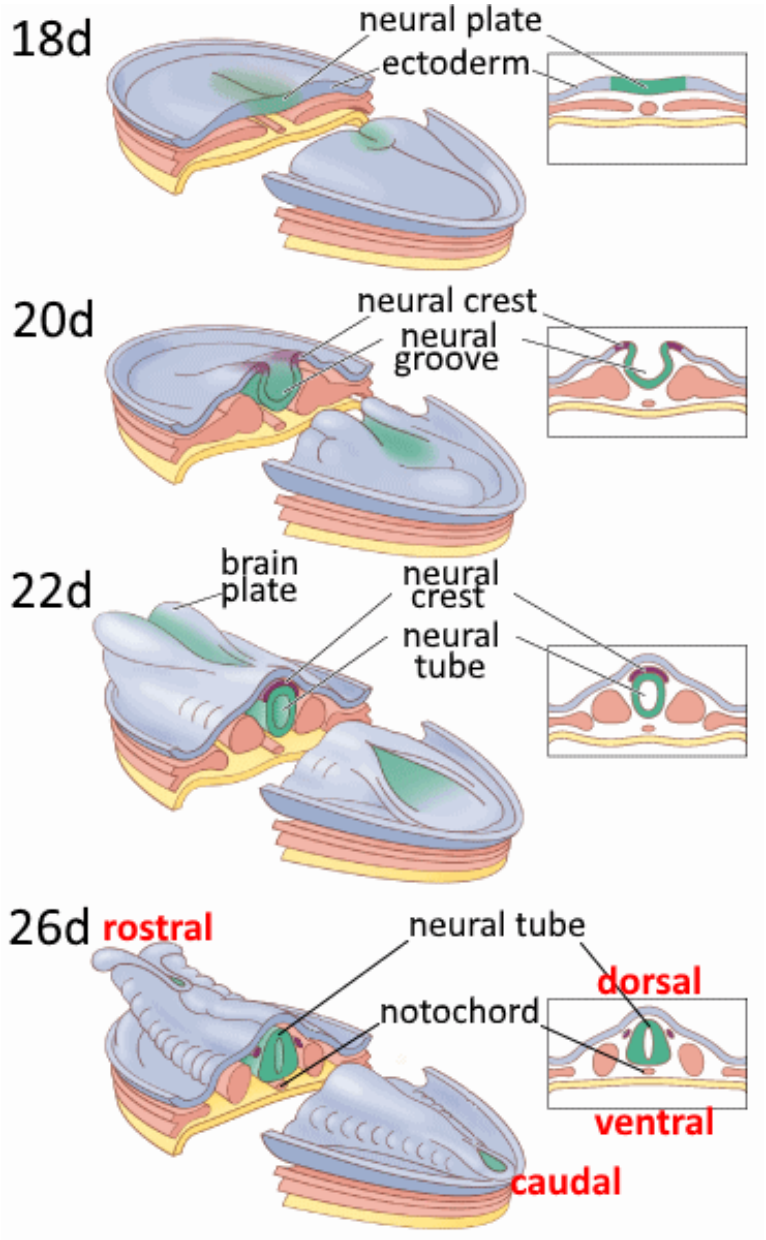

Figure 2: Formation of the neural tube from an infolding of the neural plate. The directional terms are indicated in red. Taken from [16].

On directions in the neural tube

In all following descriptions, it will be important to give directional information. We will term the future brain end of the neural tube the *rostral* end (Lat. *rostrum* - beak) and the future spinal cord end the *caudal* end (Lat. *cauda* - tail). Accordingly, the axis along the length of the neural tube (even under deformation and bending) will be

described as the *rostrocaudal* axis.
The cross-sectional profile will be labeled *dorsal* (Lat. *dorsum* - back) at the part that resides near the ectoderm directly after neurulation, and *ventral* for those cells closer to the endoderm. Again, these terms will still be used under future deformation of the surroundings and the axis describing this transversal profile will be termed *dorsoventral*. The directional terms are also indicated in the last image of Figure 2.

The neural tube after closure

During further development, cells at the most dorsal and most ventral poles along the tube differentiate into *floor plate* (ventral) and *roof plate* (dorsal) cells (from 17d on) [15]. As we will explain in the next section, both plates function as signaling sources for the differentiation of cells along the dorsoventral axis. Along the rostrocaudal axis, spatially heterogeneous cell proliferation, arising constrictions in the tube wall as well as different signals cause the formation of three distinct brain vesicles (Figure 4) [1] : the *forebrain* (*prosencephalon)*, the midbrain (*mesencephalon*) and the hindbrain (*rhombencephalon*). Cells from these vesicles are the ancestors of the adult (fore-, mid- and hind-) brain tissue. For a long time it was believed that the caudal neural tube will give rise to the spinal cord. However, substantial evidence pointing towards distinct origins for spinal cord and rostral neural tube cells has accumulated [17]. During further development, the tube does not keep its shape but undergoes a number of conformational changes such as different flexures and formation of varicosities [5].
The formation and subdivision of the neural tube is the result of a network of intracellular signals that are released across the tube and the location-specific reaction of cells to these signals. We are going to set up a simple model of this system. The current knowledge on its details will be summarized in section 2.3.

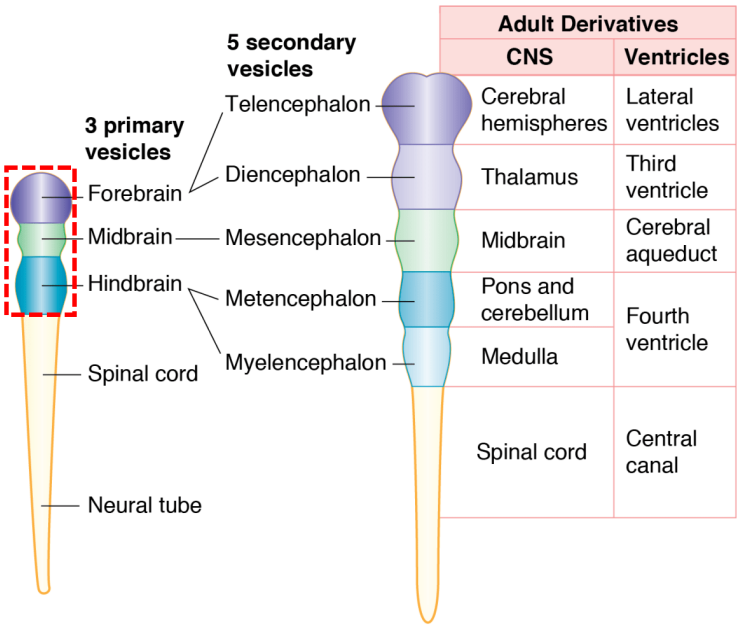

Figure 3: Subdivisions and derivatives of the neural tube. We are going to simulate the part indicated in red - the brain. Taken from [18].

2.2 Gene Regulatory Networks and Morphogen Gradients

In order to understand neural tube subdivision there are some elementary questions we need to answer first. How do single cells control their genetic expression and their phenotype? And how do they 'know' in what way they should exert this control? The following paragraphs will elucidate the biological mechanisms that solve these problems.

2.2.1 Transcriptional Regulation and Gene Regulatory Networks

The fundamental carriers of all our genetic material are deoxyribonucleic acid molecules or *DNA*. All hereditary information on the structure and organization of our bodies is encoded in our DNA. According to the central dogma of molecular biology, cells follow this 'blueprint' by firstly *trancsribing* the encoded information into mRNA (messenger ribonucleic acid) and secondly by *translating* the mRNA, synthesizing the encoded protein which can go on to e.g. be used as a building block for the cell [5].
The multitude of different cell functions and phenotypes in our organism could provoke the thought that each cell must possess an individual building plan, meaning individual DNA – this is however not the case: all cells within an organism carry the same DNA. Instead, the DNA encodes information on *all* cells and the readout of that information is controlled by *transcriptional regulation*: only certain genes (sequences of DNA) are

read out and translated into proteins, i.e. *expressed*. Cell specialization (or *differentiation*) results from the specific combination of upregulated and downregulated gene expression [19].

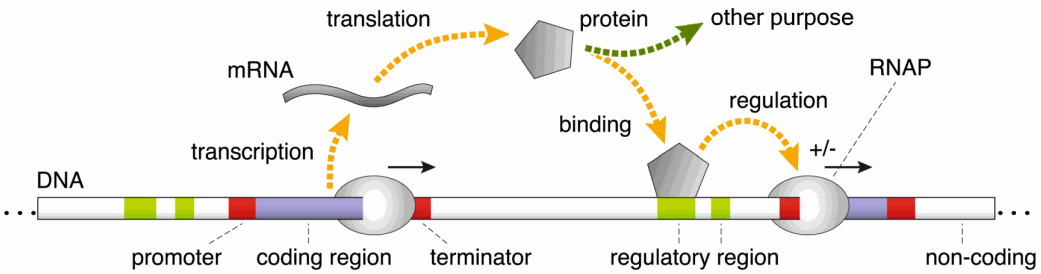

Figure 4: Simplified visualization of transcriptional regulation. RNA polymerase reads the coding region of a gene and transcribes it into mRNA (transcription). Information from mRNA is then decoded to synthesize a protein (translation). Depending on the protein it will either go on to fulfill other, e.g. structural, purposes in the cell or act as a transcription factor and regulate the expression of downstream genes. Taken from [19].

This process is controlled by transcriptional regulators called *transcription factors* that can activate or repress the readout of genes by docking to the DNA (see Figure 4). They are also proteins that are encoded in genes and built by transcription and translation, which means that the expression of one gene can regulate the expression of another *or even itself*.
Gene expression is thus subject to often highly complex orchestration systems of activation and repression circuits which we call *gene regulatory networks* (GRN). We can model these networks using ordinary differential equations and experimental data, allowing us to understand the logic behind the differentiation process. Two of these mathematical models will be used in this project.

2.2.2 Morphogen Gradients

Some transcription factors function as signaling molecules that diffuse or are actively transported across many cells from a localized source, leading to gradient-dependent different responses. These signaling molecules are called *morphogens* [5]. Morphogen gradient controlled gene expression is one of the main processes responsible for tissue patterning, not only in embryonic but also in adult development. Often, multiple overlapping gradients basically create a coordinate system where different spatial components are identified and influenced by the combination of morphogen concentrations

and the duration of exposure to them in that location [20]. For example, in neural induction alone, the morphogens *noggin*, *chordin*, *follistatin* and *fibroblast growth factors* (FGF) are involved.
Interestingly, there are certain proteins that will be used repeatedly in different developmental patterning processes at various time points, often as part of a modular circuit with a conserved working principle [21]. The most commonly found morphogens in embryonic as well as adult tissue development are FGF, *bone morphogenic protein* (BMP), members of the *hedgehog* family (in case of this thesis, *sonic hedgehog* (SHH)), WNT (a concoction between *Drosophila Wingless* and mammalian *Int1* proto-oncogene protein)) and *retionic acid (RA)* [5]. Both SHH and WNT will reappear in the GRN models discussed below.

It is important to note that cell fate is also the result of present external factors such as tissue stiffness and cell-specific factors that depend on the cell's history. For example, a cell that had a prior exposure to a morphogen might have synthesized different surface receptors and could thus react differently to a signal than one that did not get exposed. In this way, cells possess a kind of memory of earlier signals and can even react differently to the same signal just depending on time of exposure.

2.3 Neural Tube Patterning Networks

The discovery and application of molecular markers exposed a spatial heterogeneity in genetic expression across the neural tube that occurs during development long before a change in phenotype can be observed. We call the process of development of this heterogeneity the *patterning* process. It is the fundament for later differences in neuronal cell morphology, axonal trajectory, neurotransmitter content, synaptic specifity, surface labels and synaptic connection [15].

Rostrocaudal neural axis polarity is established very early in embryonic development: the endoderm releases anteriorizing signals even before gastrulation [15], and some sources even argue that fore-, mid- and hindbrain progenitors are visible already before neurulation [13]. It is confirmed that shortly after neural induction, the mesodermal and endodermal cells surrounding the neural groove release a number of signals to initiate the formation of regionally appropriate progenitor cells of the brain vesicles as well as the spinal cord. After neural tube closure, signals are also released from the floor or the roof plate within the tube. With further development even more locally released gradients define additional specification. We are going to focus our model on

the formation of the functionally specific domains for the brain shortly after neural tube closure, at the beginning of the fourth week after fertilization (around day 23). Research has shown that patterning occurs along the rostrocaudal and the dorsoventral axis and that cell identity is fairly uniform along the third axis [15], which is why it will not be discussed in the following paragraphs.

2.3.1 Rostrocaudal Patterning

When the neural tube is fully formed, secondary sources within the tube help to refine the pattern. The MHB is one of them, as well as the *Anterior Neural Ridge* (ANR) at the head of the embryo and the *Zona limitans intrathalamica* halfway in between the two (see figure 5 B). The MHB releases WNT and FGF, where WNT stimulates cell division and maintains FGF expression [1], while FGF induces midbrain and forebrain identity. FGF is also secreted from the ANR. The ZLI, just as the floor plate, emits SHH, yielding different rostrocaudal responses due to the prepatterning. This is the process we are going to simulate. Our description includes only the main signaling agents. A more detailed tabular overview is given the appendix 7.1.1.

While this part will not be included in our model, it is very important to state that rostrocaudal patterning starts already with neurulation. Initially, the neural plate cells all possess rostral forebrain character [22]. Patterning of the neural groove along the rostrocaudal axis is first initialized by signals from mesodermal and endodermal tissues siding the groove [1]. The caudal mesoderm releases WNT, while the rostral mesoderm cells secrete WNT inhibitors, building up a rostrally decreasing WNT-gradient along the tube. Together with anti-BMP agents also emitted from the caudal mesoderm, posterior neural fate is induced according to the gradient [15]. This prepatterns the groove with distinct transcription factor domains (OTX2 for future forebrain and midbrain, GBX2 for the hindbrain, see Figure 5 A) and establishes the midbrain-hindbrain boundary (MHB or *Isthmic Organizer*), where Engrailed (EN) is expressed [1].

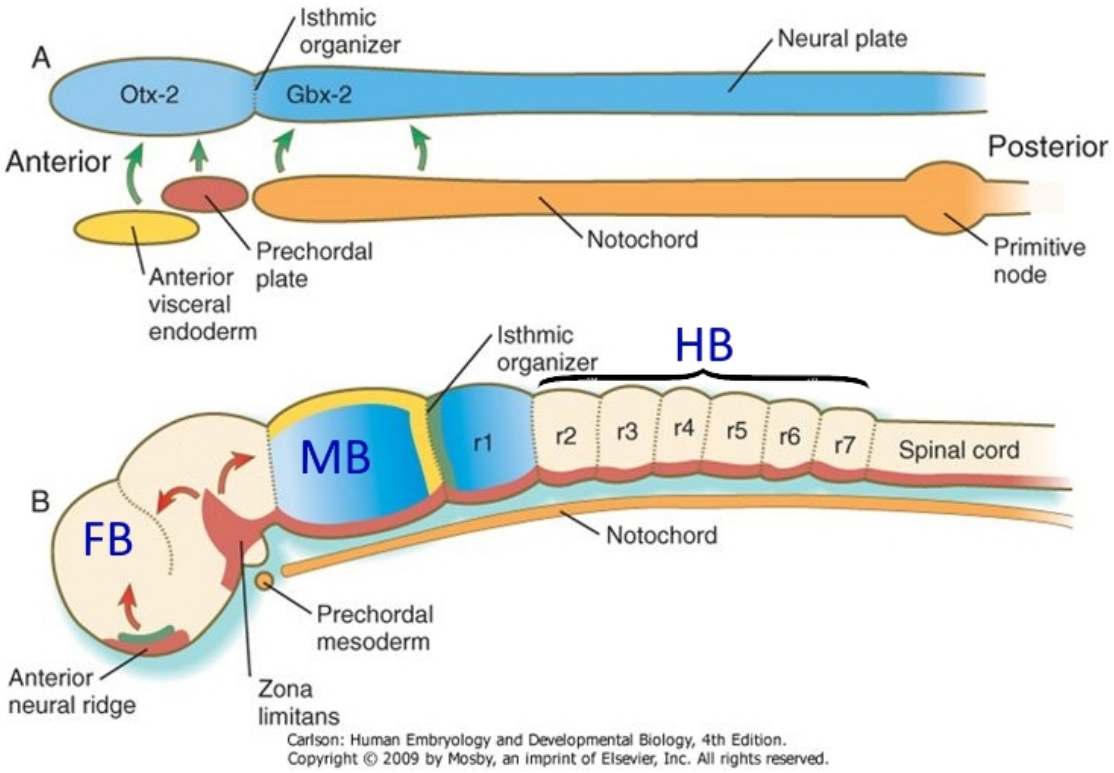

Figure 5: Signaling sources in rostrocaudal patterning [23]. *A*. Signaling from surrounding tissue leads to distinct gene expression and thus predestination of prospective brain and spinal cord cells. *B*. The most noteworthy morphogen sources involved in rostrocaudal patterning of the closed neural tube. The briain regions are marked: FB - forebrain, MB - midbrain, HB - hindbrain.

In 2012, *Kirkeby et al.* ([8]) succeeded in deriving neural progenitors from all sections of the rostrocaudal axis by inhibiting GSK3, which can equate to either activation of WNT or FGF signaling [24]. On the other hand, it has been shown that FGF concentration has very little effect on brain patterning in human embryonic stem cells [25] [26]. The conclusion is that among the different morphogens mentioned above, rostrocaudal patterning is mainly determined by WNT signaling [27].

2.3.2 Model For A Rostrocaudal Patterning Network

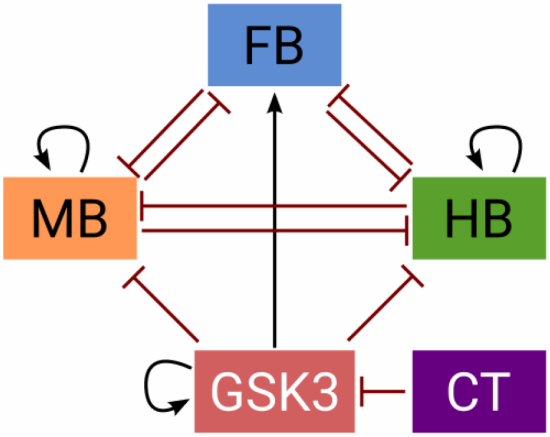

Figure 6: Proposed model for a simple regulatory network describing rostrocaudal patterning by *Balaskas et al.*. Arrows denote activation, T-shapes suppression. Taken from [28].

A simple mathematical model for an early rostrocaudal brain patterning GRN was proposed by *Brambach et al.* [28] in 2018 to explain the effects of GSK3-inhibition explored by *Kirkeby et al.* [8]. The model evaluated the formation of mid-, fore- and hindbrain cells (characterized by the gene expression of *FOXG1* (forebrain - FB), *EN1* (midbrain - MB) and *HOXA2* (hindbrain - HB) respectively) in reaction to GSK3-suppression by CHIR99021 (CT). Representative genes were chosen according to the correlation of their expression over varied levels of CT. After optimizing network topology (the result, a tristable switch, is displayed in Figure 6) as well as parameters to fit experimental gene expression levels from human embryonic stem cells, they found the following set of ordinary differential equations:

$$
\begin{aligned}
\frac{d[\mathrm{FB}]}{dt} &= \frac{c_1[\mathrm{GSK3}]^{n_1}}{1 + c_1[\mathrm{GSK3}]^{n_1} + c_2[\mathrm{MB}]^{n_2} + c_3[\mathrm{HB3}]^{n_3}} - \delta_1[\mathrm{FB}] \\
\frac{d[\mathrm{MB}]}{dt} &= \frac{c_4[\mathrm{MB}]^{n_4}}{1 + c_4[\mathrm{MB}]^{n_4} + c_5[\mathrm{FB}]^{n_5} + c_6[\mathrm{HB}]^{n_6} + c_7[\mathrm{GSK3}]^{n_7}} - \delta_2[\mathrm{MB}] \\
\frac{d[\mathrm{HB}]}{dt} &= \frac{c_8[\mathrm{HB}]^{n_8}}{1 + c_8[\mathrm{HB}]^{n_8} + c_9[\mathrm{FB}]^{n_9} + c_{10}[\mathrm{MB}]^{n_{10}} + c_{11}[\mathrm{GSK3}]^{n_{11}}} - \delta_3[\mathrm{HB}] \\
\frac{d[\mathrm{GSK3}]}{dt} &= \frac{c_{12}[\mathrm{GSK3}]^{n_{12}}}{1 + c_{12}[\mathrm{GSK3}]^{n_{12}} + c_{13}[\mathrm{CT}]^{n_{13}}} \\
\frac{d[\mathrm{CT}]}{dt} &= 0
\end{aligned}
\tag{2.1}
$$

The parameters c_i, δ_i, n_i were fitted to experimental data and can be found in appendix section 7.2.

2.3.3 Dorsoventral Patterning

Patterning along the dorsoventral axis (Figure 7) is mainly controlled by opposing signaling gradients of WNT/BMP from the roof plate and SHH from floor plate cells. Research has shown that retinoic acid signaling from surrounding tissue is also involved to some degree [29]. Floor plate signaling is first induced by external SHH-signaling from the notochord, a thin cylindrical structure along the midline of the embryo ventral to the neural tube. So far, eleven different resulting progenitor cell types have been identified by their genetic makeup [30].

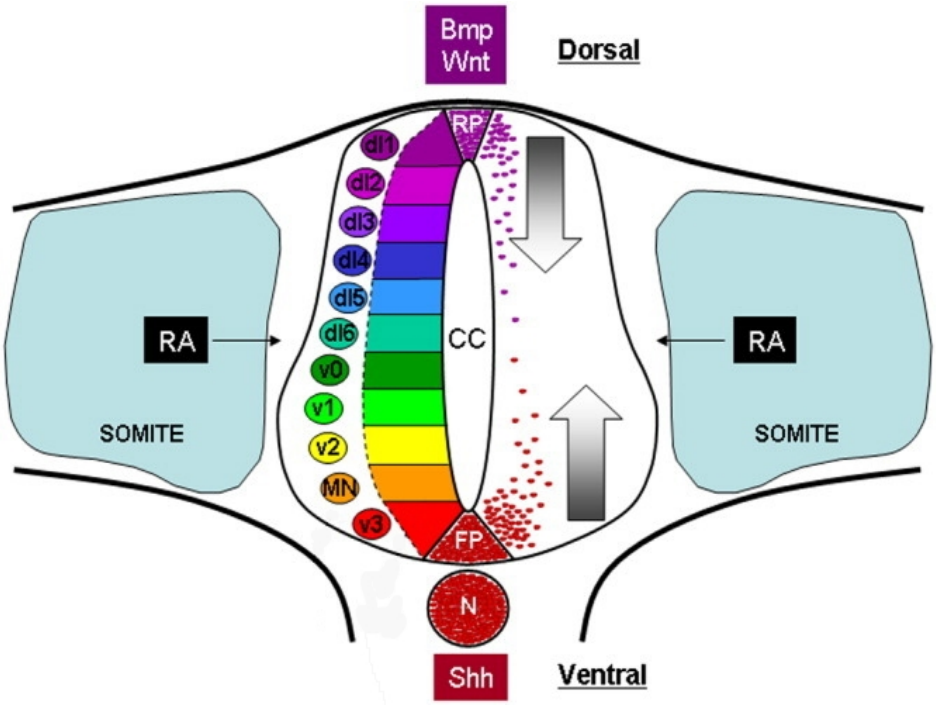

Figure 7: Dorsoventral patterning of the neural tube. Morphogen gradients from roof plate (RP) floor plate (FP) and Notochord (N) as well as retinoic acid (RA) signals from surrounding tissue control the patterning into eleven neural progenitor subtypes. Taken from [29].

2.3.4 Model For A Dorsoventral Patterning Network

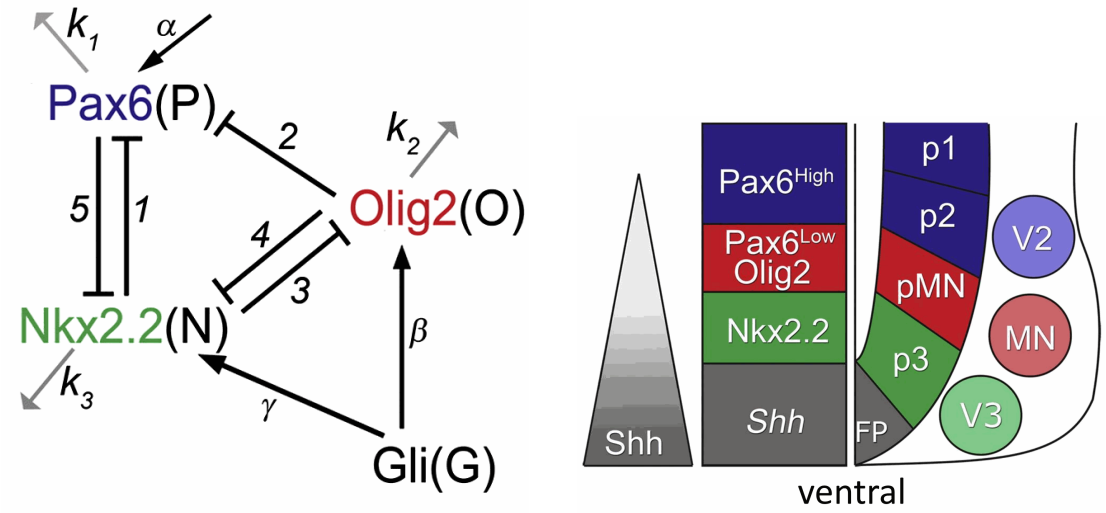

(a) (b)

Figure 8: a: Proposed model for a regulatory network defining the dorsoventral patterning by Balaskas et al. Arrows denote activation, T-shapes suppression. b: Expected patterning of the network. Both taken from [31].

In 2012, *Balaskas et al.* suggested a GRN to explain Shh-guided ventral progenitor domain formation in the neural tube. They used an *in vivo* reporter for Gli transcription factors (which are the intracellular signaling effectors of Shh, see section 7.1.3) in mouse embryonic stem cells to monitor the influence on domain development. Three domains, marked by the expression of their characteristic genes, were taken into account: the p3 domain (high *Nkx2.2* expression - N), the pMN domain (*Olig2* - O) and the p2 domain (*Pax6* - P). The resulting network structure (figure 8a) was again obtained by fitting and optimizing the reporter fluorescence intensity and is described by a set of ordinary differential equations:

$$\begin{aligned}
\frac{dP}{dt} &= \frac{\alpha}{1+\left(\frac{N}{N_{critP}}\right)^{h1}+\left(\frac{O}{O_{critP}}\right)^{h2}} - k_1 P \\
\frac{dO}{dt} &= \frac{\beta G}{1+G}\cdot\frac{1}{1+\left(\frac{N}{N_{critO}}\right)^{h3}} - k_2 O \\
\frac{dN}{dt} &= \frac{\gamma G}{1+G}\cdot\frac{1}{1+\left(\frac{O}{O_{critN}}\right)^{h4}+\left(\frac{P}{P_{critN}}\right)^{h5}} - k_3 N
\end{aligned} \tag{2.2}$$

Parameters were fitted to experimental data and can be found in appendix section 7.2.

3 Results And Discussion

3.1 Unifying The Networks

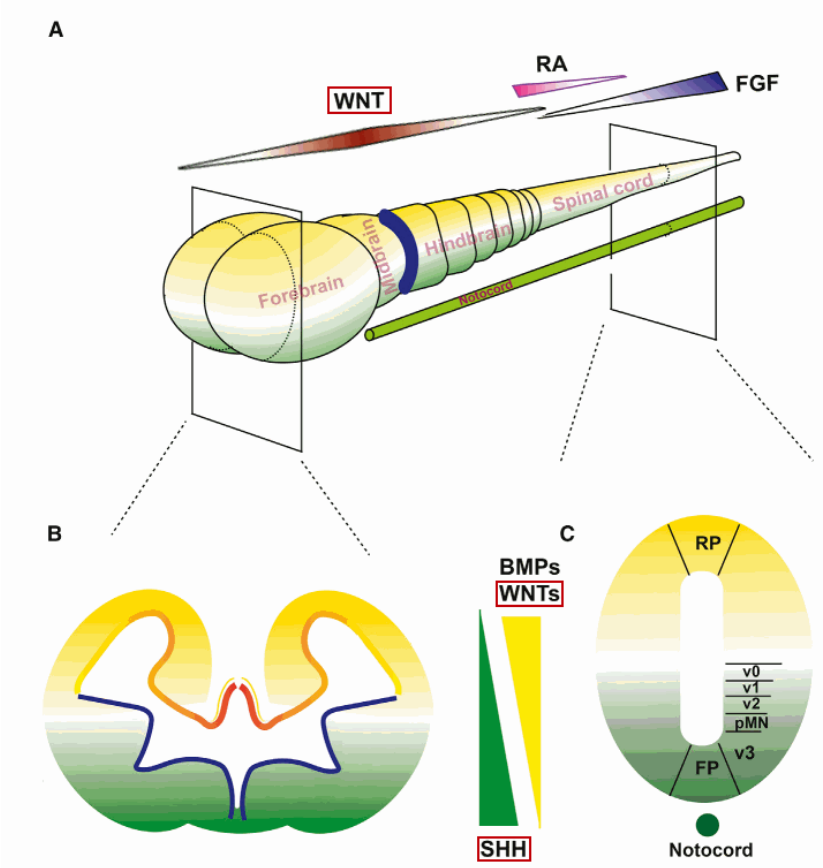

Figure 9: Patterning of the neural tube along both axes. WNT is a common node for both patterning processes. Taken from [27].

As shown in the sections on rostrocaudal and dorsoventral patterning, WNT signaling is a common denominator in both processes. We wish to model the patterning behaviour in 3D where both networks react to the same secreted WNT signals (figure 9).
Since there are currently no GRN models on rostrocaudal patterning of the entire length of the neural tube, we are only going to focus on early brain patterning. Dorsoventral patterning is highly conserved along the entire length of the tube [15]. The decision to only focus on the brain is also supported by recent evidence saying that spinal cord progenitor cells seem to have distinct origins from brain progenitor cells [17]. Research has also suggested that signals other than WNT seem to be of higher importance for spinal cord patterning [27]. The caudal end of the neural tube is also prepatterned differently even before neurulation [1] and receives further patterning signals only from exterior sources [15]. This collective evidence points to stark differences between spinal

cord and brain cell progenitors, arguing against an inclusion in our simulation.
The task at hand is now to integrate a node for WNT in both networks. In the following we will argue that this is possible without changing the networks' parameters.
Brambach et al.'s GRN was constructed in response to CT, a GSK3-inhibitor, which is evidently not WNT. However, looking at the canonical WNT pathway (see appendix 7.1.2) we can see that GSK3-suppression hinders formation of the axin degradasome, which is exactly what WNT does in the canonical cascade. By this argument we will replace the CT-node in the given network by a WNT-node with the same parameters.
Balaskas et al.'s model explains ventral domain formation due to a SHH signal, which was quantified by the amount of Gli activity in the cells (see appendix 7.1.3). However, Gli proteins are also affected by WNT signaling [32] – in fact, it has been proposed that antagonistic actions of WNT over SHH on Gli determine dorsoventral patterning [29]. According to this argument, we will introduce two nodes for SHH (activator) and WNT (repressor) into the network.
The full network is shown in Figure 10.

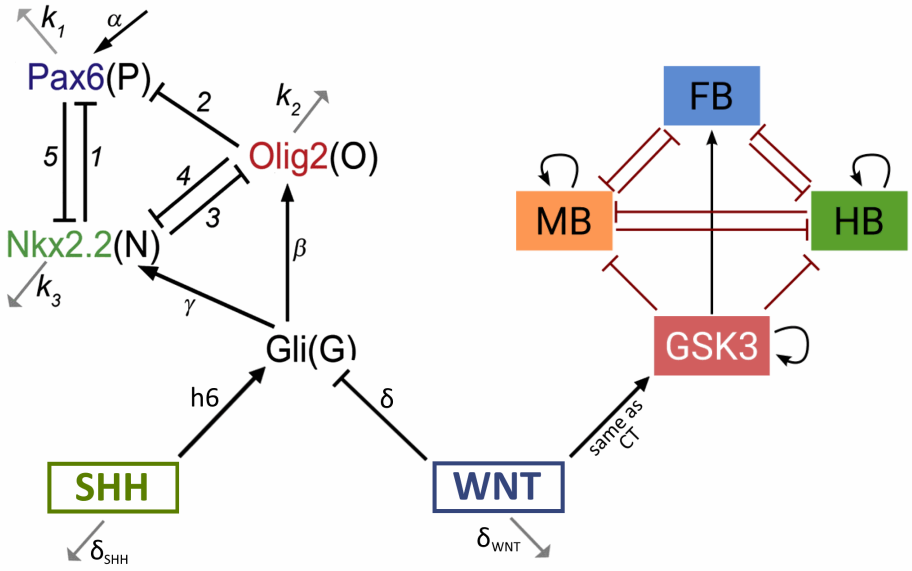

Figure 10: The unified network. The CT-node in *Brambach et al.*'s network is directly replaced with WNT.

We now have to introduce a 4th equation describing the time evolution of Gli under suppression of WNT and activation of SHH to equations 2.2:

$$\frac{dG}{dt} = \frac{\delta S}{1+S} \cdot \frac{1}{1+\left(\frac{W}{W_{critG}}\right)^{h6}} - k_4 G \tag{3.3}$$

WNT- and SHH-concentrations (not in the points of secretion) will both be described by a diffusion equation with a degradation term:

$$\frac{d[\text{WNT}]}{dt} = D_{WNT} \triangle [\text{WNT}] - \delta_{WNT}[\text{WNT}] \tag{3.4}$$

$$\frac{d[\text{SHH}]}{dt} = D_{SHH} \triangle [\text{SHH}] - \delta_{SHH}[\text{SHH}] \tag{3.5}$$

We achieved the best patterning results for the set of parameters displayed in Table 1, their derivation is explained in section 5.3. Calculation of the diffusion coefficients is discussed in 5.2.

δ	$h6$	W_{critG}	δ_{WNT}	δ_{SHH}	WNT_0	SHH_0	D_{SHH}	D_{WNT}
5.0(1.0)	1.0	1.0	0.1	0.002	2.0	1.0(5.0)	133.4	150.7

Table 1: Working set of parameters for equations 3.3 - 3.4 as well as maximum secretion levels WNT_0 and SHH_0.

3.2 Simulation Tool

All following results were obtained using the developed simulation tool, which was written in Python using mainly the Numpy and Matplotlib library modules. The simulator was designed to work in conjunction with *MagicaVoxel* [33], a free voxel editor software. This allows us to replicate reaction-diffusion mechanisms on an arbitrary three-dimensional volume with user-defined locations of signal secretion. In preparation of a simulation, the intended shape is created with MagicaVoxel and the desired points of secretion are either painted or added to the surface of volume, where the colour's value regulates the relative level of secretion (see Figure 11). One can then export the data point cloud (.ply format) and read it into the python program, in which equations, parameters and the secretion times are defined. The program outputs 3D Numpy arrays that are turned into 3D plots as well as 2D slice plots of morphogen level and gene expression.

3.3 Simplified Tube Model

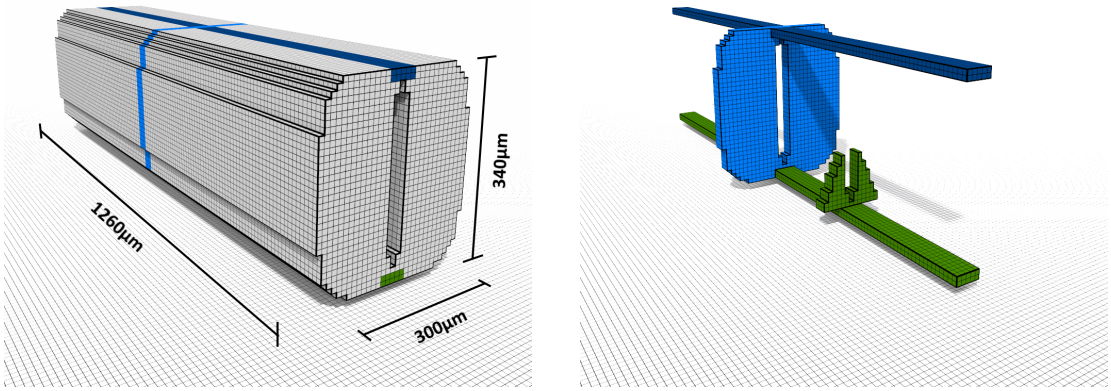

(a) (b)

Figure 11: A simple model of the anterior neural tube and most relevant secretion points, including floor plate (bottom green rod), roof plate (top blue rod), midbrain-hindbrain boundary (blue O-shape) and Zona Limitans intrathalamica (green triangle shape). a: Neural tube with secretion areas. b: Only secretion areas (Green - SHH, Blue - WNT). Images created using [33].

As explained above, we identified four signaling sources that are most relevant in patterning the anterior neural tube: floor plate cells, ZLI, roof plate cells and midbrain-hindbrain boundary, where the former two secrete SHH and the latter two release WNT. We designed a simplistic model (Figure 11) that includes these areas, combining findings from sources cited in the background as well as some preliminary tests for the specific locations. Each voxel represents a cell of length 10μm - it is however sufficient to downscale the model by 50% for our purposes, as demonstrated in Figure 12. This reduces computation time significantly. Scaling was done in *MagicaVoxel* using the built-in function *scale* with a factor of 0.5 and applied in all following results.

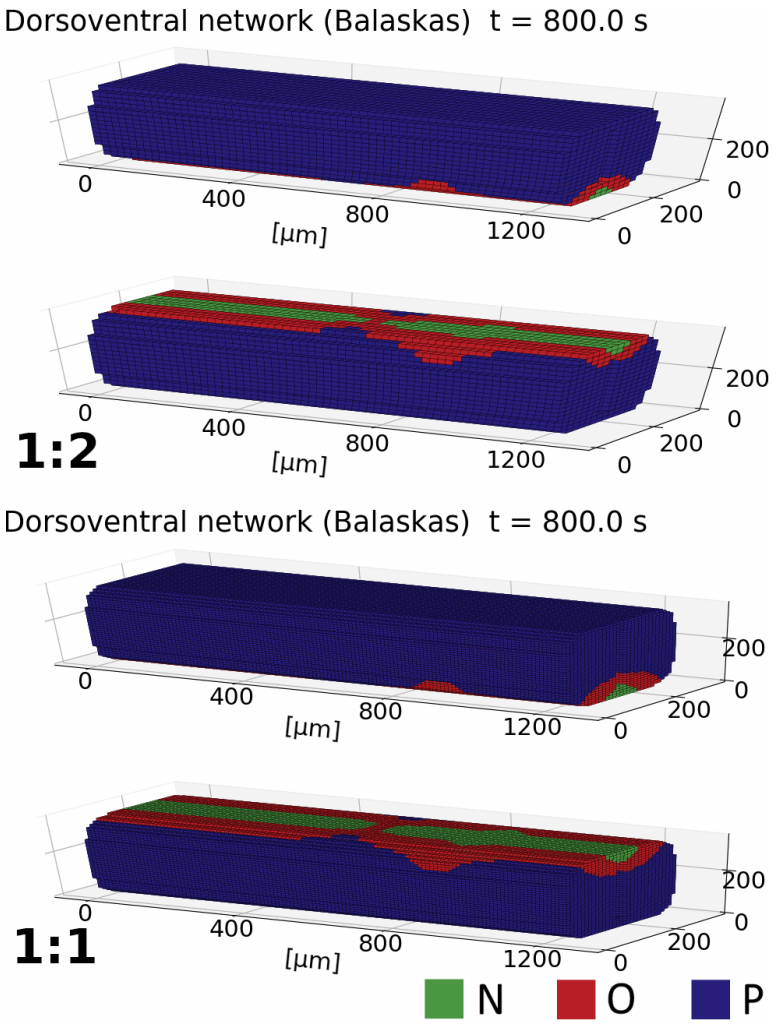

Figure 12: Comparison of patterning between the original (1:1) and the downscaled (1:2) model with reference parameters. The relevant results are conserved. (The 1:1 model might appear darker due to the higher voxel density.)

3.4 Simulation With Simplified Tube Model

For best visibility, the voxel 3D graphs in the following only display the gene most expressed in each voxel, while the 2D slices also take the level of that expression into account. For the slices, normalization is done according to the maximum level of the specific gene (and happens after comparison between the different genes). Three-dimensional plots of the dorsoventral network will be displayed from the normal perspective as well as mirrored on the xy-plane for easier evaluation.

Dorsoventral Patterning

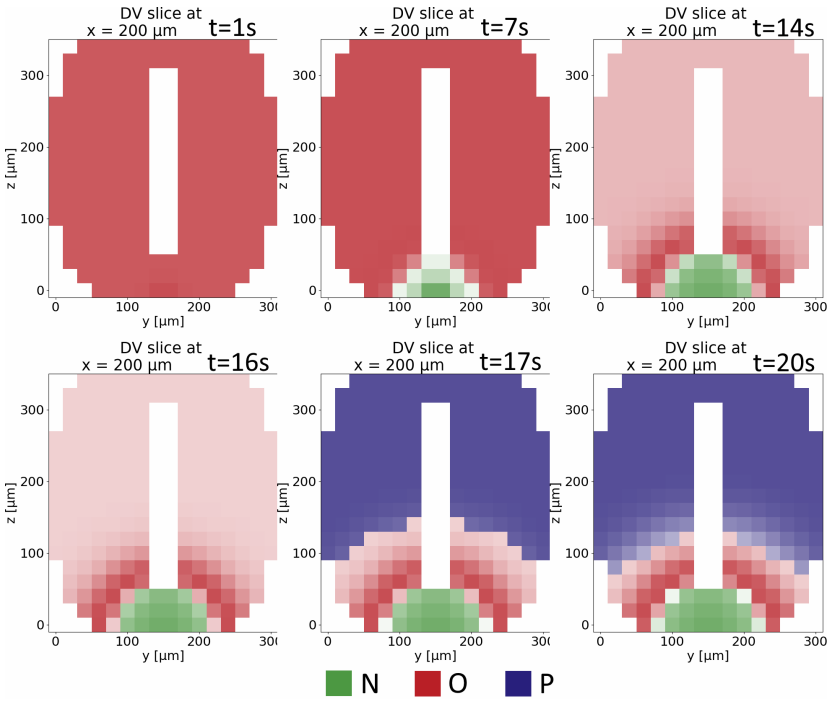

Figure 13: Early dorsoventral patterning. The pattern is established within few seconds.

Dorsoventral patterning establishes very quickly within less than a minute of model time (Figure 13) and stabilizes within a few minutes (Figure 14). The balancing process can be compared to *in vivo* gene expression (Figure 15): In both cases, the O-domain shrinks over time due to the antagonistic action of the opposing gradients of SHH and WNT. The time scale of the natural process seems however to be a lot higher, namely in the order of hours, compared to minutes in our simulation (unfortunately there is no literature available on patterning experiments with such a high time resolution).

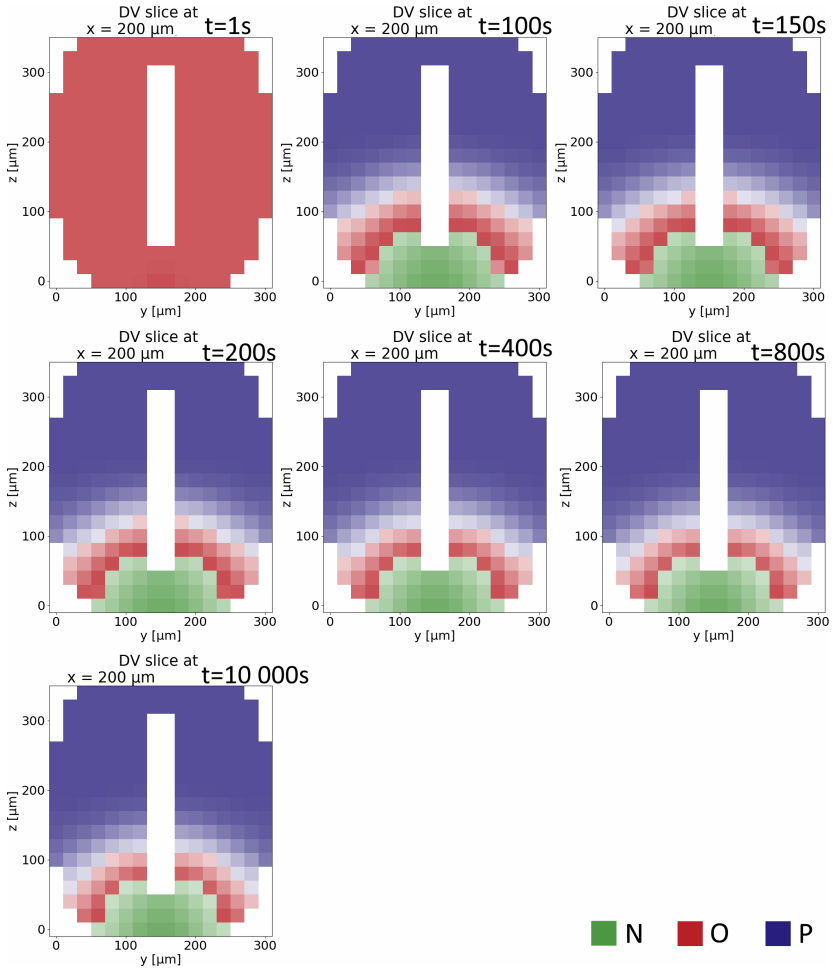

Figure 14: Dorsoventral patterning at different time points. The reduction of width of the O-domain over time can also be observed *in vivo*, see Figure 15.

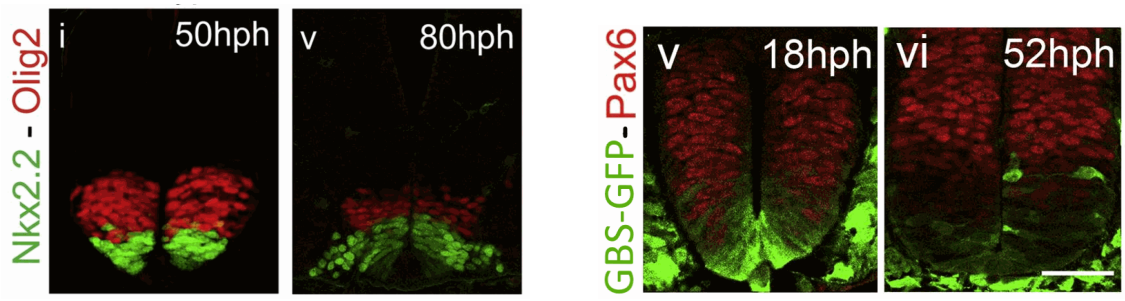

(a) (b)

Figure 15: a: *In vivo* change of N- and O-expression at different time points (hph = hours post headfold). b: *In vivo* change of P-expression (red) and Gli activity (green) at different time points. Taken from [31].

The time development for dorsoventral patterning is shown in a 3D plot in Figure 16. The combination of antagonistic signaling from zona limitans intrathalamica and the midbrain-hindbrain boundary results in an interesting variation of the width of N- and O-domains, where the pattern is almost pinched off at the midbrain-hindbrain boundary and flares out in the midbrain. This is strongly resemblant of brain vesicle restriction structure. We conclude that, counterintuitively, dorsoventral patterning might be one of the directing factors in brain vesicle restriction formation along the rostrocaudal axis.

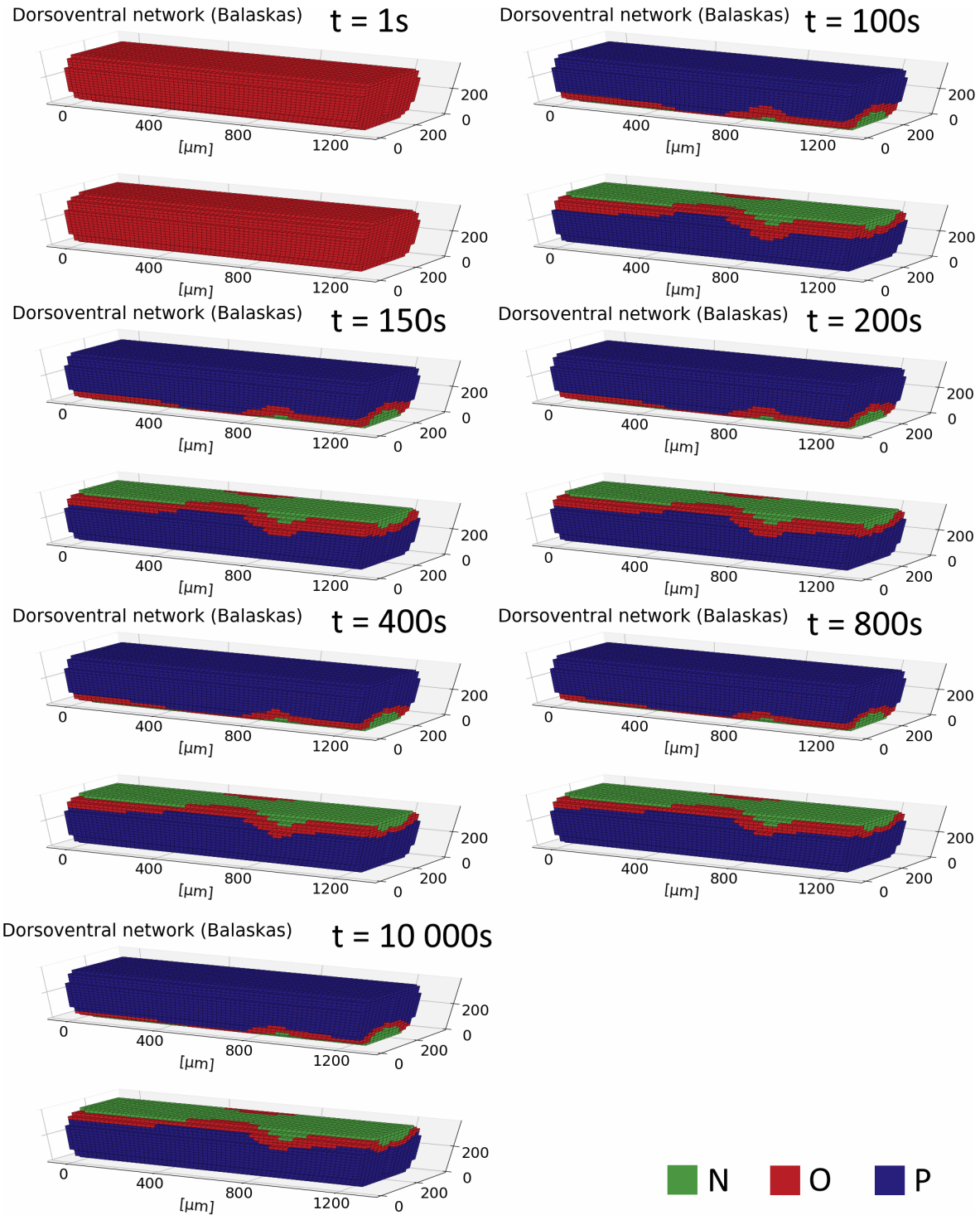

Figure 16: Dorsoventral patterning at different time points. For better visibility, the tube is also displayed mirrored in the xy-plane.

The presence of WNT does not only regulate the size of the O-, and, very lighty, the N-domain. Due to the geometry of the tube we also observe a rounding effect on the domain shape (Figure 17) in that the domains near the tube outside boundary are

pushed further ventrally than the domains near the tube lumen.

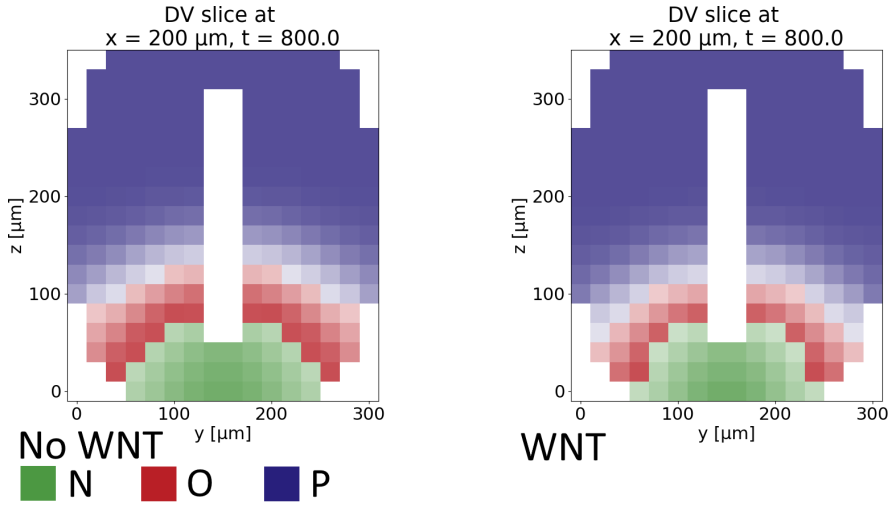

Figure 17: Influence of WNT on dorsoventral patterning.

Overall, we have confirmed the network defined in section 3.1 works very well as a stable model for dorsoventral patterning, even when extended to incorporate WNT and SHH signaling. The temporal stability we detected in particular was something *Balaskas et al.* explicitly optimized for by incorporating cell sensitivity change due to exposure time. The model does, however, only include three of the eleven known progenitor subtypes along the dorsoventral axis. In order to achieve an even more accurate view of the system and to be able to make predictions on *in vitro* differentiation it would be of great interest to extend the model to include more types.

Rostrocaudal Patterning

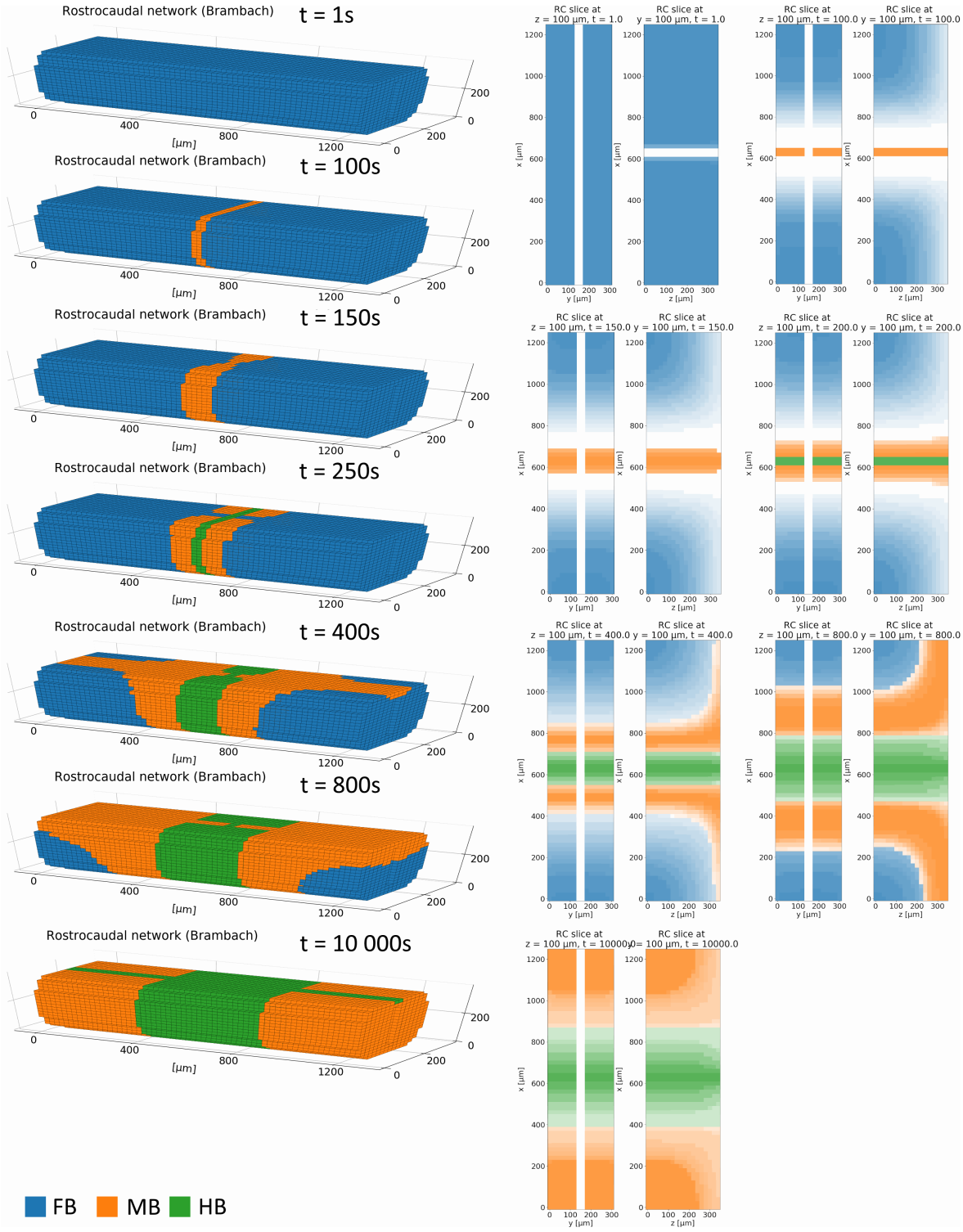

Figure 18: Rostrocaudal patterning at different time points. The patterning does not reach a stability due to the low WNT-degradation. However, low WNT-degradation was needed to achieve mid- and hindbrain patterning in the first place.

The results of the patterning process along the rostrocaudal axis are shown in Figure 18. The caudal end of the tube (left in the pictures) can be neglected since we do not include any more caudalizing signals. As discussed in section 5.3, in order to achieve a realistic patterning it was necessary to set the WNT-degradation rate very low. As a consequence, the ratio between secretion and degradation is slightly imbalanced toward the former. This is why, even though correct patterning is achieved at t = 800s, the process does not reach stability.

There are different conclusions we can draw from this: One possibility is that the neural tube boundaries are permeable so that WNT does not accumulate inside the tube. However, this would entail WNT signaling outside the tube, possibly disturbing other processes. While we could not find any evidence supporting such a process or permeability in the literature, this might be worth researching experimentally in the future.

Another option would be to adapt *Brambach et al.*'s network to time of exposure, which has not been done so far. One could also argue that since both SHH and WNT morphogens have very similar parameters (see section 5.2) and serve a similar function, the degradation coefficients should also be alike. In that case, an adaptation of the rostrocaudal network would also be necessary, since the right patterning is not achieved by changing other parameters (section 5.3). On the other hand, a WNT-degradation coefficient similar to that of SHH would also mean a neglibile influence of WNT on ventral patterning. This contradicts evidence for a dominance of WNT in dorsoventral patterning [29].

Finally, we cannot neglect that the processes we are modelling are biological. There may be hidden variables that we have not included in our framework, for example, it is possible that cells start to produce morphogen-destructor proteins at a certain exposure level or that they release domain-retaining signals. Furthermore, there are important variables we actually do know of but which we disregard, such as the prepatterning explained in section 2 or other signaling factors such as BMP. In order to control for these problems, it would be important to acquire exact *in vivo* rostrocaudal patterning images with a high time resolution.

For the reasons discussed above, we can conclude that the *Brambach et al.* model part of our network is valid for only a restricted amount of model time.

3.5 Simulation With Realistic Tube Model

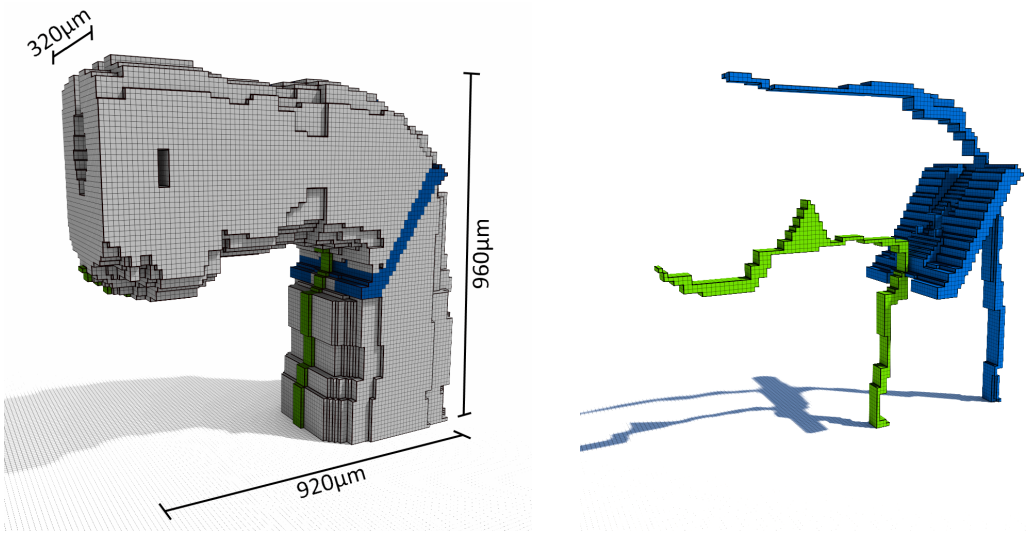

(a) (b)

Figure 19: A more realistic model of neural tube geometry. a: Neural tube with secretion areas. b: Only secretion areas (Green - SHH, Blue - WNT). Images created using [33].

In order to study the effects of tube geometry on patterning, we also repeated the simulation on a more realistic tube model shown in Figure 19. The structure was designed after a lifelike three-dimensional embryonic model [11].

In the case of dorsoventral patterning, depicted in Figure 20, we observe a pronounced rounding effect on the N- and O- expression domains for the areas in which the ventral tube side is thicker. Aside from that, just as in the simplistic model, the patterning remains conserved along the whole tube. The vesicle-reminiscent structuring seems slightly less pronounced, which could be explained by the fact that the model geometry already includes beginnings of vesicle formation.

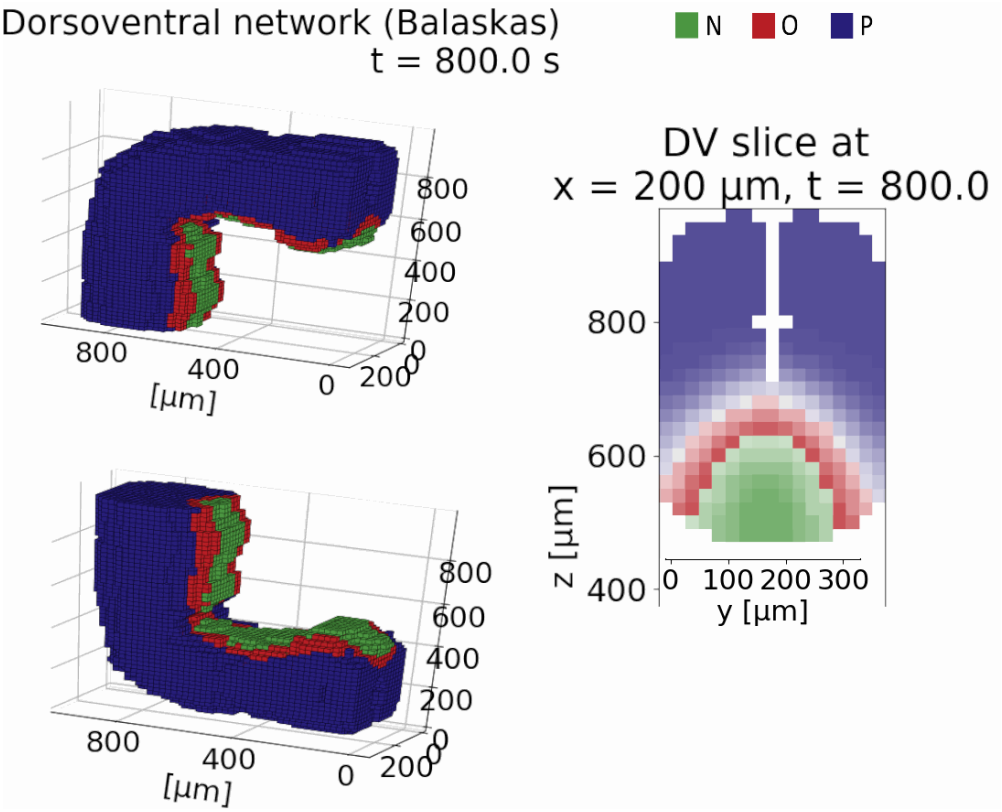

Figure 20: Dorsoventral patterning with the realistic model.

In rostrocaudal patterning, shown in Figure 21, the curved geometry impacts mainly the hindbrain domain structure. In contrast to the simplistic model, hindbrain gene expression is maintained almost up to the rostral end of the tube. This could be a physical reason for the flexures of the neural tube mentioned in section 2. It is also very interesting to note that the curving achieves a *dorsoventral* patterning with mid-, hind- and forebrain genes in a part of the rostral tube. Circling back to the application in *in vitro* cell differentiation, this could be a very important result determining the combination of genes we need to express in order to produce e.g. dopaminergic neurons.

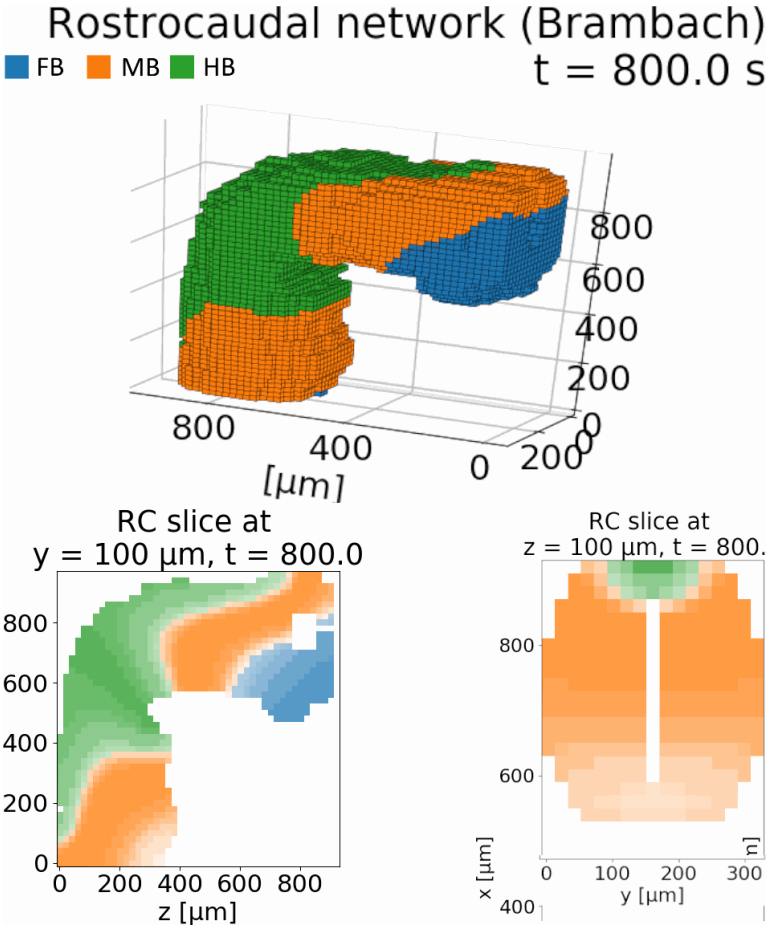

Figure 21: Rostrocaudal patterning in the realistic model.

4 Conclusion

In this project, we have successfully implemented a three-dimensional model of neural tube patterning. We achieve patterning within a restricted timeframe and are able to hypothesize several interesting ideas on this basis. We identified a possible correlation between dorsoventral patterning and vesicle formation as well as some areas in which fore-, mid- and hindbrain expression are actually stacked dorsoventrally. In order to confirm these hypotheses, more experimental data with better time-resolution is needed on neural tube patterning. This would also be beneficial for setting up a temporally adapted version of the rostrocaudal network which is most definitely necessary. The dorsoventral part of the networks could be extended to include more of the 8 remaining dorsoventral progenitor types. Before the implementation of these measures it is not easy to make predictions on *in vitro* differentiation behaviour.

Future steps for optimizing the computational model could entail for example to include finite voxel volume (so that signaling levels cannot become indefinitely high) or cell migration, apoptosis and division. In its current state, the program is however already a useful tool in determining the influence of secretion and geometry on reaction-diffusion processes.

5 Methods

5.1 Computational Methods

5.1.1 Discretized Laplace Operator

To solve the diffusion part (see 5.1.2) of the GRN equations numerically, it is necessary to find a discretized approximation for the Laplacian

$$\triangle_N u(x_1, ..., x_N) = \sum_{i=1}^{N} \frac{\partial^2 u}{\partial x_i^2} \tag{5.6}$$

Where $\triangle_N$ is the N-dimensional laplacian and u is some function, e.g. a concentration, depending on the position $(x_1, ..., x_N)$ (a scalar field). For the simplest case of only one dimension ($N = 1$), Taylor expanding $u(x)$ to second order yields

$$u(x + a) = u(x) + a\frac{\partial u}{\partial x} + \frac{1}{2}a^2\frac{\partial^2 u}{\partial x^2} + \mathcal{O}(a^3) \tag{5.7}$$

Also,

$$u(x - a) = u(x) - a\frac{\partial u}{\partial x} + \frac{1}{2}a^2\frac{\partial^2 u}{\partial x^2} + \mathcal{O}(a^3) \tag{5.8}$$

By neglecting the higher order terms and adding 5.8 and 5.7 we can find the *finite difference approximation* for the Laplacian in one dimension:

$$\triangle_1 u(x) = \frac{\partial^2 u}{\partial x^2} \approx \frac{u(x - a) - 2u(x) + u(x + a)}{a^2} \tag{5.9}$$

If we discretize the function $u(x)$ on a mesh of lattice constant a, so that $x = ja$ for every point x (where j is some integer) and consequently $u(x) = u(ja) =: u_j$, we can express 5.9 as

$$\triangle_1 u|_j \approx \frac{u_{j-1} - 2u_j + u_{j+1}}{a^2} \tag{5.10}$$

In two dimensions, the Taylor expansion looks like this:

$$u(x + a_x, y + a_y) \approx u(x, y) + a_x\frac{\partial u}{\partial x} + a_y\frac{\partial u}{\partial y} + \frac{1}{2}a_x^2\frac{\partial^2 u}{\partial x^2} + \frac{1}{2}a_y^2\frac{\partial^2 u}{\partial y^2} + a_x a_y\frac{\partial^2 u}{\partial x \partial y} \tag{5.11}$$

Which yields the discretized Laplacian for $N = 2$:

$$\triangle_2 u|_{j,k} \approx \frac{u_{j-1,k} - 2u_{j,k} + u_{j+1,k}}{a_x^2} + \frac{u_{j,k-1} - 2u_{j,k} + u_{j,k+1}}{a_y^2} \tag{5.12}$$

If we choose a square lattice for the discretization, $a_x = a_y = a$ this becomes

$$\triangle_2 u|_{j,k} \approx \frac{u_{j-1,k} + u_{j+1,k} + u_{j,k-1} + u_{j,k+1} - 4u_{j,k}}{a^2} \tag{5.13}$$

By analogous reasoning, in three dimensions we have

$$\triangle_3 u|_{j,k,l} \approx \frac{u_{j-1,k,l} + u_{j+1,k,l} + u_{j,k-1,l} + u_{j,k+1,l} + u_{j,k,l-1} + u_{j,k,l+1} - 6u_{j,k,l}}{a^2} \tag{5.14}$$

[34]

5.1.2 Matrix Method and Sparse Matrix Handling

The equations one wishes to model in this project are reaction-diffusion type equations of the form

$$\frac{du(\mathbf{x})}{dt} = \underbrace{D \triangle_3 u(\mathbf{x})}_{\text{Diffusion part}} + \underbrace{f(u(\mathbf{x}), v(\mathbf{x}), ...)}_{\text{Reaction part}} \tag{5.15}$$

within a certain constricted volume (where u and v are different reactants). The shape of the volume does not affect the reaction part as it is not influenced by any spatial component other than that exactly in $\mathbf{x}$. However, it is evident that the diffusion into one compartment will be influenced by the surrounding compartments, a process which we approximated in equation 5.14. We will therefore treat the diffusion part of the equation on its own in the following and discuss how to model an arbitrary shape. (In fact, diffusion and reaction can also be implemented as two separate computational steps within the same simulated time step.)
Consider for the sake of clarity the 2D diffusion case. As we are going to discuss in more detail in 5.1.3, we are going to apply the *explicit Euler* method, i.e. we are looking to compute

$$u^{n+1}(x) = (Dh \triangle_2 + 1)u^n(x) \tag{5.16}$$

with arbitrary no-flux boundary conditions (*Neumann boundaries*)

$$u^n_{i_1,j_1} - u^n_{i_1-1,j_1} = 0 \tag{5.17}$$
$$u^n_{i_2,j_2} - u^n_{i_2-1,j_2} = 0 \tag{5.18}$$
$$u^n_{i_2,j_2-1} - u^n_{i_2,j_2} = 0 \tag{5.19}$$
$$... \tag{5.20}$$

. To this end, it can be useful to transform 5.16 into a matrix equation

$$\mathbf{u}^{n+1} = (\mathbb{1} + \frac{Dh}{a^2}\mathbf{A})\mathbf{u}^n \tag{5.21}$$

Where the vector form $\mathbf{u} = (u_1, ..., u_{N_c})$ should consist of all N_c compartments in the volume (see Figure 22). The matrix $\mathbf{A}$ is then a $N_c \times N_c$ matrix where the n-th row gives the impact of the compartments surrounding compartment u_n due to the Laplacian.

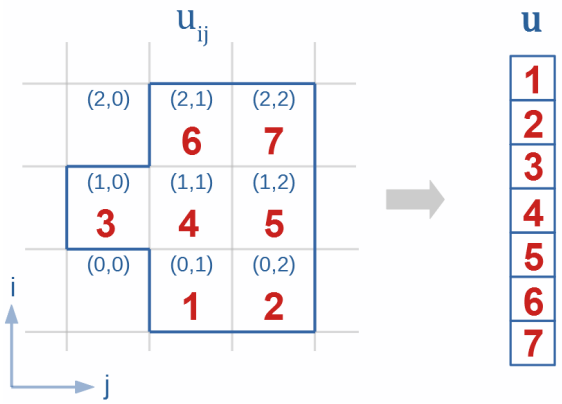

Figure 22: Arrangement of lattice points u_{ij} into a vector $\mathbf{u}$ to facilitate matrix calculations.

For a lattice point that has no Neumann (or other) boundary neighbours, e.g. u_4 in the Figures, the Laplacian takes on the discussed form (eq. 5.13) and the 4th row in $\mathbf{A}$ will look like

$$A = \begin{pmatrix} ... & & & & & & \\ 1 & 0 & 1 & -4 & 1 & 1 & 0 \\ ... & & & & & & \end{pmatrix} \leftarrow \text{4th row}, \tag{5.22}$$

since the Laplacian stencil (Figure 23a) covers only other neighbouring points within the volume.

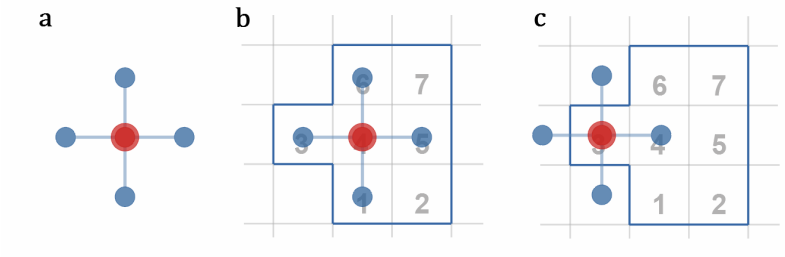

Figure 23: a: Laplacian stencil in 2D. b: Laplacian applied to a lattice point without boundary neighbours. c: Laplacian applied to a lattice point with Neumann boundaries.

If we consider a compartment near Neumann boundaries, e.g. u_3 (Figure 23c), we find that the boundary conditions

$$\begin{aligned} u_{3\uparrow} - u_3 &= 0 \\ u_{3\leftarrow} - u_3 &= 0 \\ u_{3\downarrow} - u_3 &= 0 \end{aligned} \tag{5.23}$$

can be collected in the local diffusion equation (arrows denote the no-flux neighbouring compartment):

$$\begin{aligned} \triangle_2 u_3 &= \frac{u_{3\leftarrow} + u_4 + u_{3\uparrow} + u_{3\downarrow} - 4u_3}{a^2} && (5.24) \\ &= \frac{(u_{3\leftarrow} - u_3) + u_4 + (u_{3\uparrow} - u3) + (u_{3\downarrow} - u_3) - (4 - NB)u_3}{a^2} \\ &\overset{5.23}{=} \frac{u_4 - (4 - NB)u_3}{a^2} && (5.25) \end{aligned}$$

$$\text{where} \quad NB = \text{Nr. of Neumann boundaries} = 3 \tag{5.26}$$

Thus, the 3rd row in $\mathbf{A}$ will be

$$\mathbf{A} = \begin{pmatrix} \dots & & & & & & \\ 0 & 0 & -1 & 1 & 0 & 0 & 0 \\ \dots & & & & & & \end{pmatrix} \leftarrow \text{3rd row} \tag{5.27}$$

If we follow this scheme for the three-dimensional case, the resulting $\mathbf{A}$ will have $-(6 - NB_n)$ as the diagonal element of the nth row (cf. eq. 5.14, in 2D the 6 needs to be replaced by 2) and a 1 for each neighbouring compartment. Since the total number of elements in $\mathbf{A}$ scales with the number of compartments *squared* and the matrix is sparse (not more than 7 nonzero entries per row), *it is computationally of*

great advantage to only store the nonzero entries of $\boldsymbol{A}$ *with their corresponding indices* (n, m) *instead of saving the whole* $\boldsymbol{A}$.
In case the volume is not isolated from its surroundings and we imagine the outside compartments, e.g. in Figure 23 to have some constant concentrations c_i, so $u_{3\leftarrow} = c_1$, $u_{3\uparrow} = c_2$ and $u_{3\downarrow} = c_3$ in equation 5.24 (*Dirichlet boundary conditions*), we can collect these terms in a vector $\mathbf{b}$, so that

$$\mathbf{u}^{n+1} = (\mathbb{1} + \frac{Dh}{a^2}\mathbf{A})\mathbf{u}^n + \frac{Dh}{a^2}\mathbf{b} \tag{5.28}$$

Where in this case

$$\mathbf{A} = \begin{pmatrix} ... & & & & & & \\ 0 & 0 & -4 & 1 & 0 & 0 & 0 \\ ... & & & & & & \end{pmatrix} \qquad \mathbf{b} = \begin{pmatrix} ... \\ \sum_{i=1}^{3} c_i \\ ... \end{pmatrix} \qquad \leftarrow \text{3rd row} \tag{5.29}$$

5.1.3 Explicit Euler and Stability

Computational modelling of the given reacting-diffusion equations equates to the numerical solution of a system of coupled ordinary differential equations (ODEs)

$$\begin{aligned} \frac{du(\mathbf{x},t)}{dt} &= f_u(\triangle u(\mathbf{x},t), u(\mathbf{x},t), v(\mathbf{x},t), w(\mathbf{x},t), ...) \\ \frac{dv(\mathbf{x},t)}{dt} &= f_v(\triangle u(\mathbf{x},t), u(\mathbf{x},t), v(\mathbf{x},t), w(\mathbf{x},t), ...) \\ ... &= ... \end{aligned} \tag{5.30}$$

where $u(\mathbf{x},t), v(\mathbf{x},t), ...$ are the involved reactants. As we showed above, it is possible to turn each of these equations into a matrix equation via spatial discretization (see sections 5.1.1 and 5.1.2), so that we can write e.g.

$$\frac{d\mathbf{u}(t)}{dt} = \frac{D}{a^2}(\mathbf{A}\mathbf{u} + \mathbf{b}) + f(\mathbf{u}, \mathbf{v}, ...) \tag{5.31}$$

One way to find the time evloution of $\mathbf{u}(t)$ is now to discretize the time according to $t = nh$ (so that $\mathbf{u}(t) = \mathbf{u}(nh) =: \mathbf{u}^n$), and to then approximate the derivative on the left hand side by a forward Euler step

$$\frac{d\mathbf{u}(t)}{dt} = \frac{\mathbf{u}^{n+1} - \mathbf{u}^n}{h} \tag{5.32}$$

Since this amounts to just plugging in the definition of the derivative, one might expect this to be the natural way to go about the numerical solution of 5.31. However, it is important to first evaluate the stability of this method, i.e. we need to make sure that errors are not amplified over time. We will now show that this is *conditionally true* for the forward Euler (or *explicit Euler*) method using the *von Neumann stability analysis*. Due to the limited precision of computational number storage, any result we obtain numerically ($\mathbf{u}^n$) will differ from the exact analytical result ($\bar{\mathbf{u}}^n$) by a round-off error $\boldsymbol{\varepsilon}^n$:

$$\mathbf{u}^n = \bar{\mathbf{u}}^n + \boldsymbol{\varepsilon}^n \tag{5.33}$$

Since the time evolution of $\bar{\mathbf{u}}^n$ is given exactly by the forward Euler step, this implies that the error $\boldsymbol{\varepsilon}^n$ is subject to the same time evolution as the numerical solution $\mathbf{u}^n$ [35]. The von Neumann procedure assumes slow variations of the parameters in eq. 5.31 and periodic boundary conditions, which allows us to write the independent solutions as [36] [37]

$$\begin{aligned} \boldsymbol{\varepsilon}^n_{j,k,l} &= \xi^n e^{iq_1 j\Delta x} e^{iq_2 j\Delta y} e^{iq_3 j\Delta z} \\ &= \xi^n e^{ia(q_1 j + q_2 k + q_3 l)} \end{aligned} \tag{5.34}$$

A numerical method is said to be stable if $|\xi^n| \leq 1$, so the error does not increase under time development. For simplification reasons, we will also assume the reaction part of eq. 5.15 to be zero for the analysis.

$$\begin{gathered} \frac{du(t,x,y,z)}{dt} = D \triangle u(t,x,y,z) \\ \text{so} \\ \mathbf{u}^{n+1} = (Dh \triangle_3 + \mathbb{1})\mathbf{u}^n \end{gathered} \tag{5.35}$$

As discussed above, this also holds true for the error. We can write explicitly

$$\begin{aligned}\varepsilon_{j,k,l}^{n+1} = \Bigg[\frac{Dh}{a^2}\big(&\varepsilon_{j-1,k,l}^n + \varepsilon_{j+1,k,l}^n + \varepsilon_{j,k-1,l}^n + \varepsilon_{j,k+1,l}^n \\ &+ \varepsilon_{j,k,l-1}^n + \varepsilon_{j,k,l+1}^n - 6\varepsilon_{j,k,l}^n\big) + 1\Bigg]\varepsilon_{j,k,l}^n\end{aligned} \tag{5.36}$$

Plugging in 5.34 we find

$$\begin{aligned}\xi\varepsilon_{j,k,l}^n = \Bigg[\frac{Dh}{a^2}\big(&e^{-iaq_1}\varepsilon_{j,k,l}^n + e^{iaq_1}\varepsilon_{j,k,l}^n + e^{-iaq_2}\varepsilon_{j,k,l}^n + e^{iaq_2}\varepsilon_{j,k,l}^n \\ &+ e^{-iaq_3}\varepsilon_{j,k,l}^n + e^{iaq_3}\varepsilon_{j,k,l}^n - 6\varepsilon_{j,k,l}^n\big) + 1\Bigg]\varepsilon_{j,k,l}^n\end{aligned} \tag{5.37}$$

Dividing by $\varepsilon_{j,k,l}^n$ yields

$$\xi = \frac{Dh}{a^2}\left(\sum_{s=1}^{3}[e^{-iaq_s} + e^{iaq_s}] - 6\right) + 1 \tag{5.38}$$

Since $e^{-iaq_s} + e^{iaq_s} - 2 = 2(cos(aq_s) - 1)$, we can write this as

$$\xi = \frac{Dh}{a^2}\underbrace{\left(\sum_{s=1}^{3} 2[cos(aq_s) - 1]\right)}_{:=\lambda} + 1 \tag{5.39}$$

Each cosine in the sum can be 1 or -1 at maximum or minimum, so that $-12 \leq \lambda \leq 0$. The stability condition $|\xi^n| \leq 1$ implies

$$1 + \frac{Dh}{a^2}\lambda \leq 1 \qquad \text{and} \qquad -(1 + \frac{Dh}{a^2}\lambda) \leq 1 \tag{5.40}$$

for all q_s and thus for all λ. Both inequalities are satisfied for the trivial case, and the first one is evidently true for any $\lambda < 0$. Thus, we only need to check

$$\begin{aligned} -(1 + \frac{Dh}{a^2}(-12)) &\leq 1 \\ 12\frac{Dh}{a^2} &\leq 2 \\ \rightarrow \qquad h &\leq \frac{a^2}{6D} \end{aligned} \tag{5.41}$$

Therefore, the explicit Euler scheme in three dimensions converges if 5.41 is satis-

fied, i.e. if we pick a small enough time step h.

There are other numerical schemes that are *unconditionally stable*, such as the *implicit Euler* scheme, in which a backwards Euler step is used for the time derivative:

$$\frac{\mathbf{u}^n - \mathbf{u}^{n-1}}{h} = \frac{D}{a^2}\mathbf{A}\mathbf{u}^n \qquad \rightarrow \qquad \mathbf{u}^{n+1} = (\mathbb{1} - \frac{Dh}{a^2}\mathbf{A})^{-1}\mathbf{u}^n \tag{5.42}$$

However, these implicit schemes require inversion of $\mathbf{A}$, which becomes computationally expensive quickly for large matrices. We will therefore only make use of the explicit Euler method.

5.2 Diffusion Coefficients For Signaling Proteins

5.2.1 Estimation Of Radius Of Gyration From Protein Length

There is no literature available on the diffusion coefficients of the signaling proteins involved in our model. It is therefore necessary for us to estimate them. Fortunately, *He and Niemeyner* proposed an estimation based on the radius of gyration R_G (see below) of the protein. Unfortunately there is also very little information available on these radii. We will therefore make use of the following general estimation formula based on *Hong and Lei* [38] for physiological conditions:

$$R_G \approx 3N^{\frac{2}{5}}\text{Å} \qquad \text{(physiological conditions)} \tag{5.43}$$

where N is protein chain length (number of amino acids). Inserting the protein lengths $N_{WNT} = 370$ [39] and $N_{SHH} = 462$ [40] yields

$$R_{WNT} \approx 32\mathring{A} = 3.2nm \qquad \text{and} \qquad R_{SHH} \approx 35\mathring{A} = 3.5nm \tag{5.44}$$

5.2.2 Estimation Of Diffusion Coefficient From R_G

He and Niemeyner [41] proposed the following equation to estimate protein diffusion coefficients based on R_G and M the molecular mass:

$$D = \frac{6.85 \times 10^{-15} T}{\eta \cdot \sqrt{M^{\frac{1}{3}} \cdot R_G}} \tag{5.45}$$

where D is in $\text{m}^2\cdot\text{s}^{-1}$, T is the temperature in K, η the viscosity of the surrounding medium, M the molecular mass in $\text{kg}\cdot\text{kmol}^{-1}$ and R_G the radius of gyration in Ångström.
Inserting the molecular masses $M_{WNT} = 40.98kDa = 40980\frac{kg}{kmol}$ [39] and $M_{SHH} =$

$49.61kDa = 49610\frac{kg}{kmol}$ [40] as well as conditions the for the inside of the human body T=37°C = 310K and $\eta = 0.75$cP $= 7.5 \cdot 10^{-4}$Pa·s [28] yields together with the gyration radii from above

$$D_{SHH} = 133.4\mu m^2 s^{-1} \qquad \text{and} \qquad D_{WNT} = 150.7\mu m^2 s^{-1} \tag{5.46}$$

5.3 Parameter Tuning

In order to achieve the best possible patterning result, we performed an analysis on the system using a set of testing parameters. These initial parameters were educated guesses or based on preliminary tests and are displayed in Table 2.

δ	$h6$	W_{critG}	δ_{WNT}	δ_{SHH}	WNT_0	SHH_0	D_{SHH}	D_{WNT}
1.0	1.0	1.0	0.1	0.1	2.0	1.0	133.4	150.7

Table 2: Testing parameters for equations 3.3 - 3.4 as well as maximum secretion levels WNT_0 and SHH_0.

Initial expression levels for the network part of *Balaskas et al.* were directly adopted from the paper. For the rostrocaudal network (*Brambach et al.*), FB expression was set high due to the initial forebrain character of all cells as discussed in section 2.3.1 while MB and HB levels were set to minimal value. SHH and WNT levels were taken to be zero except in the points of secretion. A summary of all initial values can be found in Table 3. The standard maximum model time for one simulation run (800.0s) was picked in order for most systems to attain steady state or to at least display a definitive trend based on preliminary tests.

FB	MB	HB	P	O	N	G	SHH	WNT
1	0.001	0.001	0	0	0	3.0	0	0

Table 3: Initial values for the involved genes and proteins.

5.3.1 Starting Parameters

The results for a simulation run with just the testing parameters are shown in Figure 24 and 25. The morphogen levels quickly reach a steady state after less than 50s model time (see Appendix 7.3.1) in which secretion and degradation are balanced. Similarly, the network described by *Balaskas et al.* quickly switches from its initial O-expression to an almost finished patterning after only 17s. The only further change is a further retreat of the O-expression, after which a steady state is reached here as well (cf. Appendix 7.3.1).

The patterning and temporal behaviour are in good agreement with *in vivo* observations depicted in Figure 15. While there is a small but significant difference in the extent of the N-expressing area, the main deviation is in the timescale difference - the model achieves patterning within a minute, where it seems to be an hour-spanning process *in vivo* (there is currently no literature on smaller timescale experiments available).

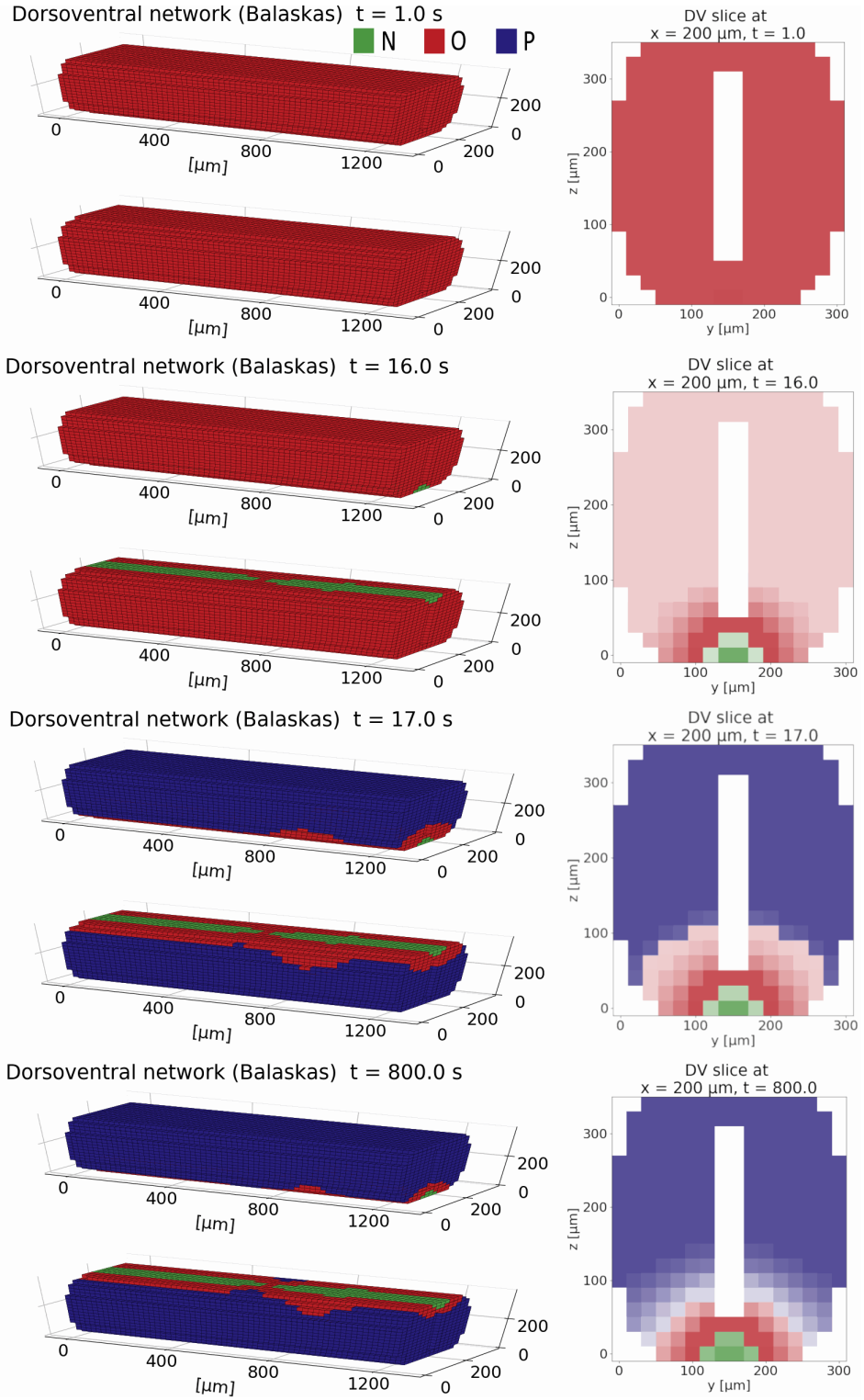

Figure 24: Evolution of dorsoventral patterning for reference parameters. Voxel 3D graphs only display the gene most expressed in each voxel. 2D slices show nuanced expression normalized to the maximum expression of the specific gene. The results are in good agreement with *in vivo* observations (Figure 15).

The simulated evolution of rostrocaudal patterning (Figure 25) is however substan-

tially different from the expected patterning. An unrealistic behaviour towards the caudal end (left in the pictures) can be neglected, since we are only considering genetic markers up to the hindbrain. For the end anterior to the midbrain-hindbrain border (right in pictures), a steady-state tripartition into the (approximately equal-sized) brain regions would be the expectation. *In silico*, the hindbrain and especially the midbrain part remain extremely small. Furthermore, the system is not reaching a steady state while reacting to a steady-state signaling gradient on this timescale (see Appendix 7.3.1) and the midbrain remains small even for long times of exposure.

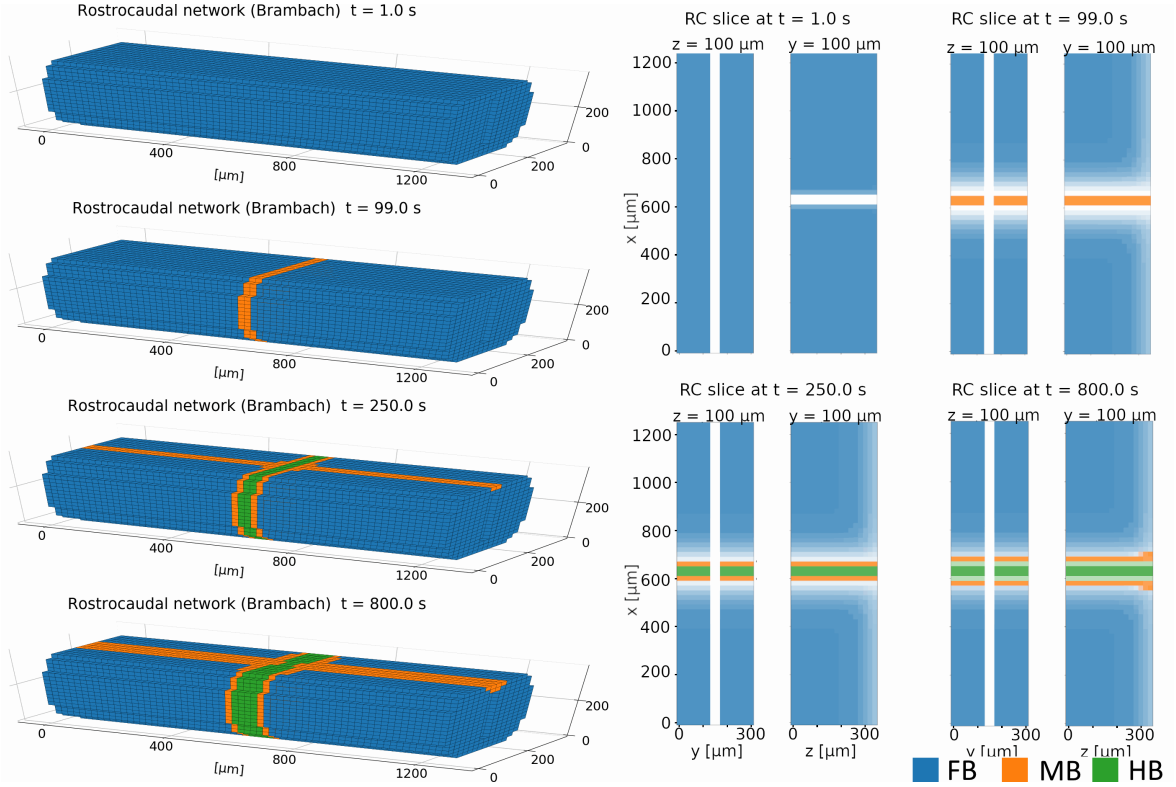

Figure 25: Evolution of rostrocaudal patterning for reference parameters. Voxel 3D graphs only display the gene most expressed in each voxel. 2D slices show nuanced expression normalized to the maximum expression of the specific gene. The results are not in good agreement with *in vivo* observations due to the thin MB and HB domains.

We have thus identified three issues with the parameters chosen for the reference simulation:

- Small HB- and especially MB-domain (rostrocaudal)
- Small N-domain (dorsoventral)
- No steady-state development in rostrocaudal network on this timescale

In the course of the following sensitivity analysis, we will explore possible sources of these problems.

5.3.2 Levels Of Signal Secretion (WNT_0, SHH_0)

One might speculate that larger expression domains for MB, HB and N could be achieved by increasing the morphogen secretion levels. Figure 26 shows however that while there is a domain-broadening effect, it is mostly impacting the cells close to the secretion sources: while HB- and N-expressing areas do become wider for higher secretion levels and narrower for lower ones, the extent of the MB- and O-domains remains about the same due to the expression thresholds of the involved networks.

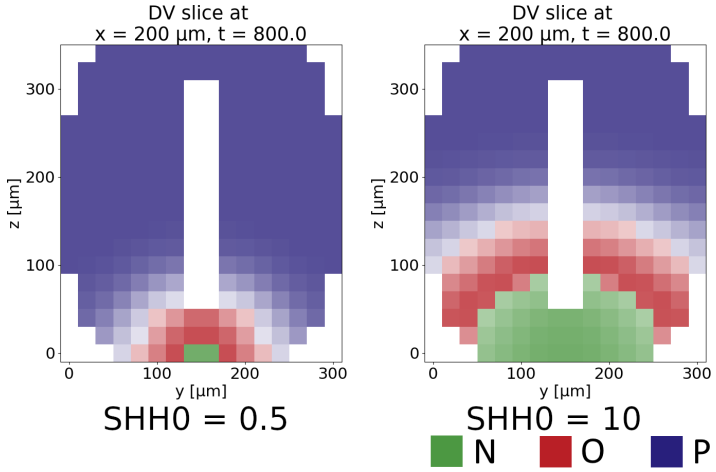

(a) SHH level impact

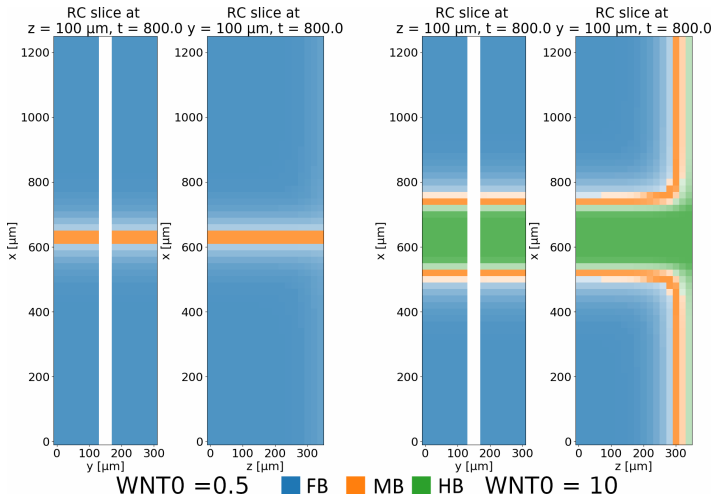

(b) WNT level impact

Figure 26: Patterning for different levels of WNT and SHH at the secretion sources.

Figure 27 illustrates another (or possibly the underlying) issue: we do not see a

difference in dorsoventral patterning between a simulation with no WNT involved and that with a high level of WNT secretion. This means that while the two networks are coupled via the equations, either the coupling of Gli to WNT is too weak (or that to SHH too strong) to affect the patterning or the range of WNT is too short to actually have a significant influence.

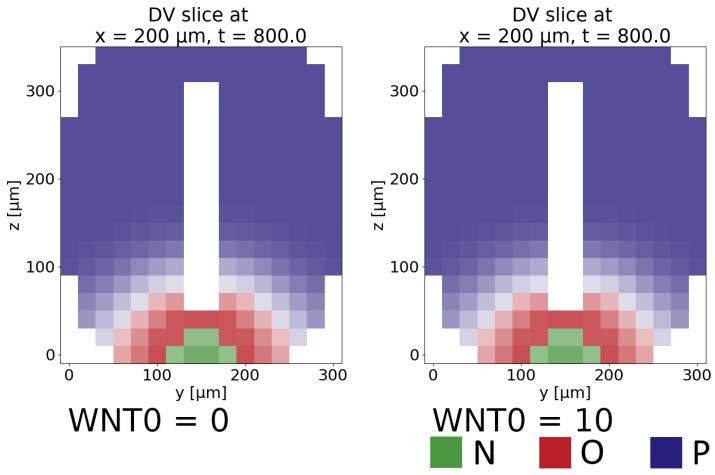

Figure 27: Dorsoventral patterning does not change for different WNT-secretion levels - the influence or the range of WNT is too insignificant with the reference parameters.

5.3.3 SHH-Gli Coupling (δ)

Let us first examine the coupling of SHH to Gli, where the magnitude of activation is controlled by parameter δ. Variation of δ yields the patterning pictured in Figure 28. Since an increase in δ corresponds to a lowering of the 'threshold amount' of SHH needed for the network to react to the signal, it is not surprising that the resulting patterning is very similar to the one obtained from raising SHH-secretion level. Since SHH and WNT are antagonists in their action on Gli, it is important to note that varying δ and SHH_0 are nevertheless not the same thing. We have thus found two different methods to increase N-domain size.

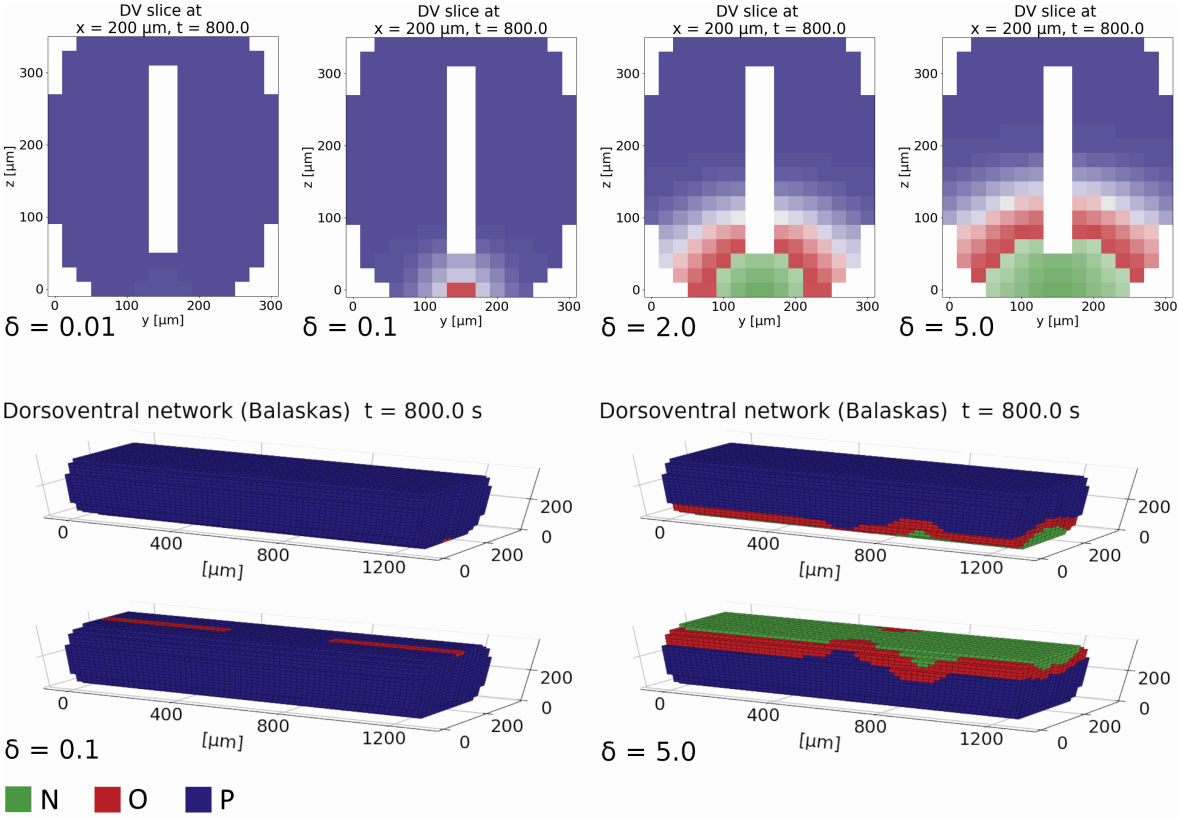

Figure 28: Dorsoventral patterning for varying values of δ, i.e. different strengths of SHH-Gli coupling.

5.3.4 WNT-Gli Coupling (W_{critG}, $h6$)

The suppressive influence of WNT on Gli is governed by the parameters W_{critG} and $h6$. The critical value W_{critG} determines the level of WNT required to induce Gli suppression and the cooperativity factor $h6$ controls the abruptness of that change (the range of values over which suppression varies from light to strong). Figure 29, displaying the effects of W_{critG} change demonstrates that, even for very low critical values, Gli-repression only occurs in proximity to the midbrain-hindbrain border - no change is visible further away from it. For variation of $h6$, the changes are minimal (cf. Appendix 7.3.1). Again, the results are most definitely a consequence of the short range of WNT morphogen signal. They do however show that the coupling in itself is working as intended. While it might be possible to achieve further optimization by varying W_{critG} and $h6$ after increasing WNT range, they do not appear to be the most crucial factor in resolving the issues identified in section 5.3.1.

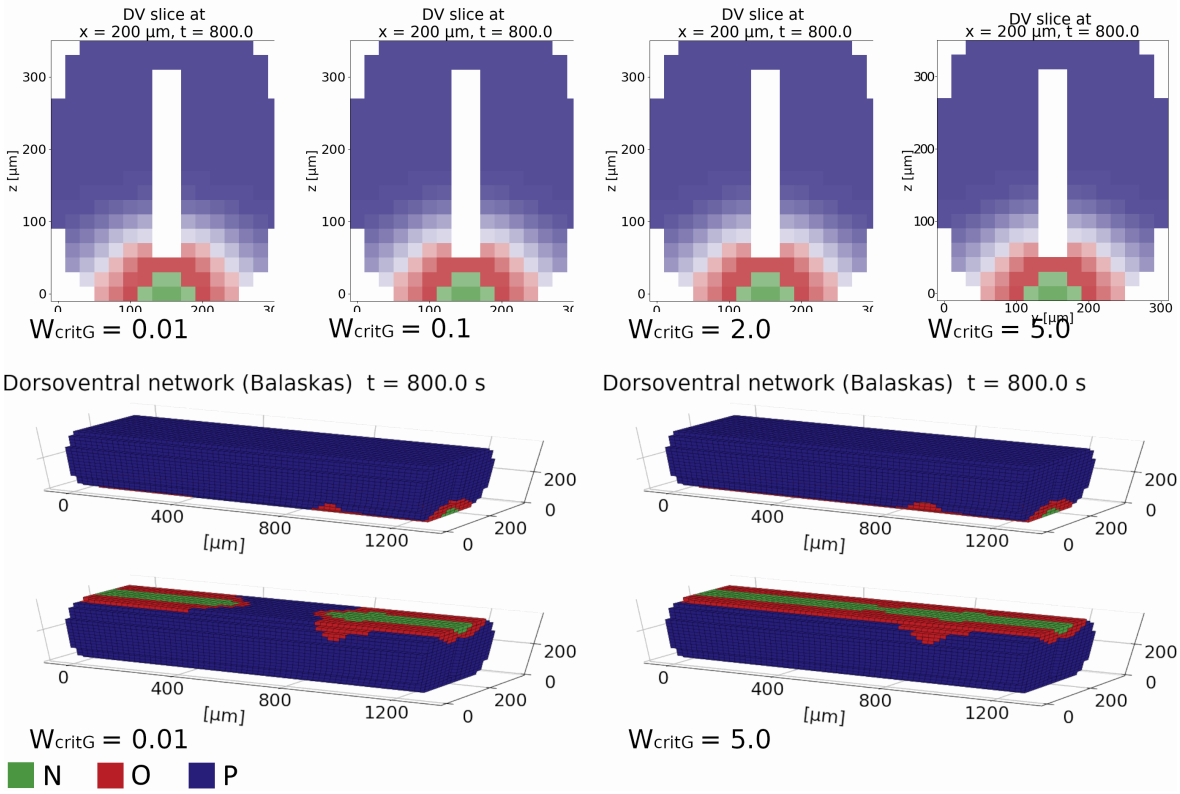

Figure 29: Dorsoventral patterning for varying values of W_{critG}.

5.3.5 Degradation Rates (δ_{WNT}, δ_{SHH})

The shape of a morphogen signal gradient is determined by the balance between secretion, diffusion and degradation of the protein. Figure 30 shows the effects of varying degradation rate δ_{WNT} at t = 800.0s on the rostrocaudal network. Both underlying morphogen gradients and the result for the dorsoventral axis can be found in the Appendix 7.3.1. In both cases, increasing morphogen range allows for effective control of intermediary (i.e. MB- and O-) domain sizes albeit accompanied by some growth of the source domains.

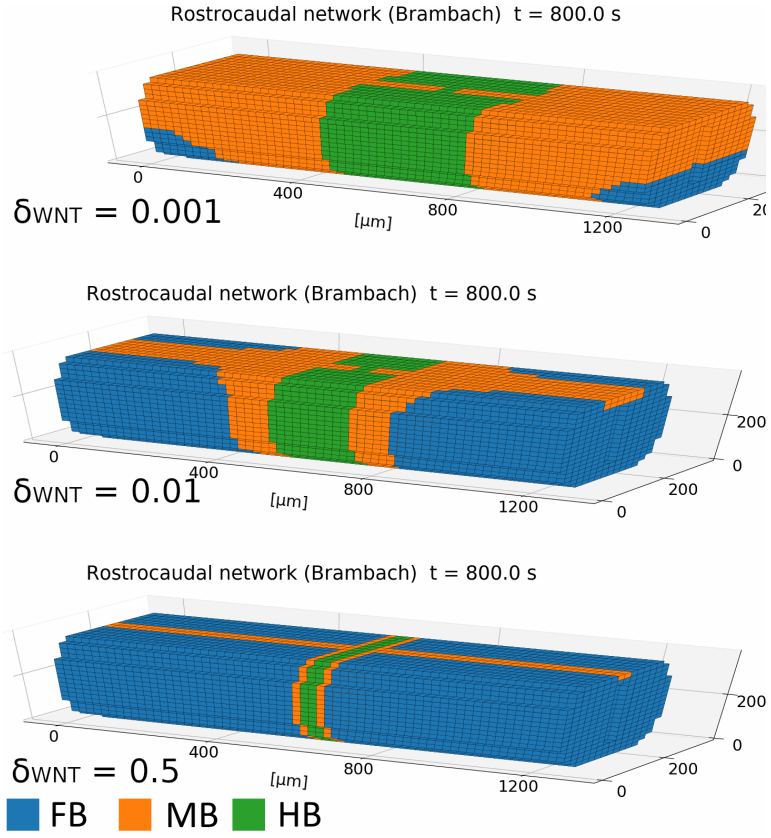

(a) 3d plot

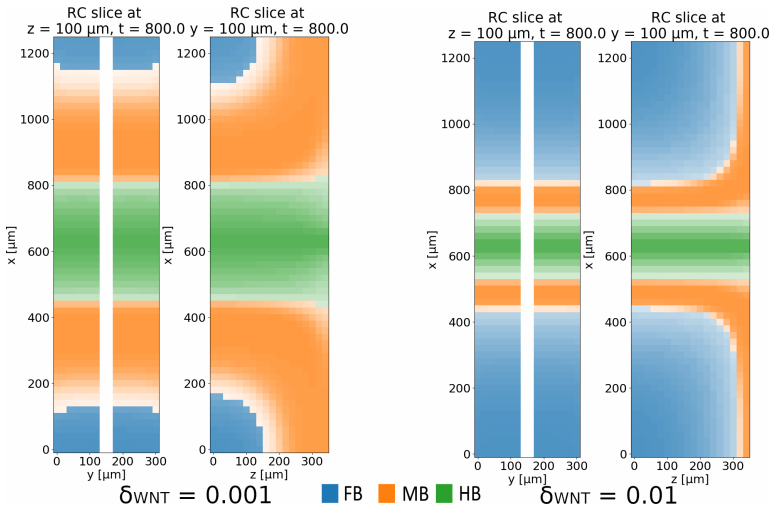

(b) 2d slices

Figure 30: Impact of variation of WNT-degradation rate δ_{WNT} on rostrocaudal patterning. These images are a snapshot at t

This behaviour can be explained by taking into account the concentration-expression graphs for the uncoupled networks (Figure 31): Only very low concentrations induce expression of FB or P, and after a certain threshold concentration, expression of HB or N will always dominate. However, in both cases, the middle state (MB or O) takes

up a proportionally large amount of the concentration range we are working at. This is why a degradation rate decrease results in slow growth of the high-concentration domains (HB and N) and faster growth of the intermediary domains MB and O.

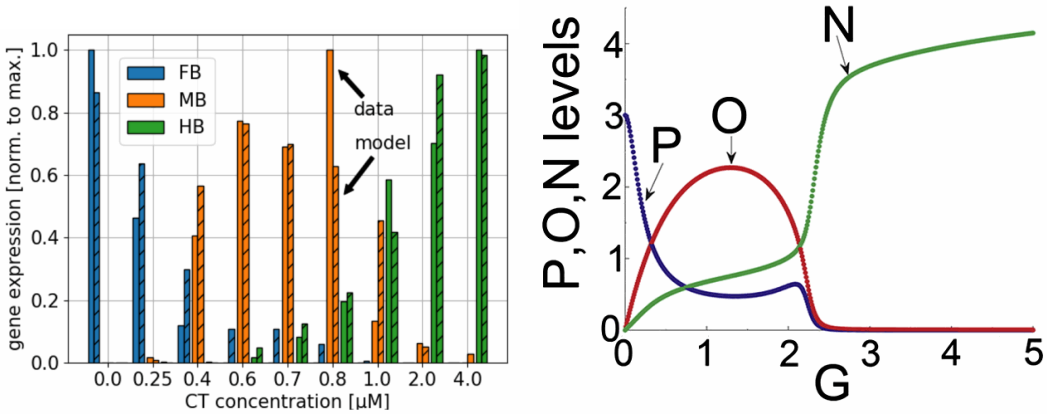

(a) Brambach et al. [28]

(b) Balaskas et al. [31]

Figure 31: Expression patterns over linear concentration gradients for the uncoupled networks.

6 Acknowledgements

I would like to thank Victor Olariu for having granted me this opportunity and guiding me through the project. It was wonderful to be allowed to work on my own terms, but knowing support was always there should I need it.

I would also like to express my thanks to Najmeh Abiri and Bosse Söderberg for helping me out with any technical difficulties.

My thanks also go out to Henrik Jönsson for providing guidance with his simulation software (even though I did not end up using it).

Many thanks to my parents and sisters for proofreading and just in general always being a great and constant source of support in my life. I want to especially thank my father for a late-night 'getting started with cloud computing' discussion and my mother for a pre-Christmas debugging session. I am so lucky not only to have wonderful parents, but incredibly smart ones at the same time. (The sisters are also alright.)

Finally, I cannot possibly thank Torsten enough for being by my side no matter what.

7 Appendix

7.1 Background

7.1.1 Signals In Rostrocaudal Patterning

Table 1 | **Boundaries in the developing vertebrate brain**

Regional interface	Cell lineage restriction	Signalling function
Anterior neural border (ANB)	?	+ (anti-WNT, FGFs)
Pallial–subpallial boundary (PSB)	+ (Ventricular zone only)	None detected
Telencephalon–diencephalon	–	None detected
Zona limitans intrathalamica (ZLI)	+ (Two boundaries with lineage restriction anteriorly and posteriorly; does not extend into roof plate)	+ (SHH, WNTs?, FGFs?)
Thalamus–pretectum	–	None detected
Diencephalic–midbrain boundary (DMB)	+	None detected
Midbrain–hindbrain boundary (MHB)	+ (Might be leaky; possibly two boundaries dorsally)	+ (FGFs, WNT1)
Rhombomeres	+ (Except floor plate; ventricular zone only)	+ (WNT1, WNT3A?, WNT8B?, WNT10B?)
Spinal cord	–	Anteroposterior: – Dorsoventral: +

FGF, fibroblast growth factor; SHH, sonic hedgehog.

Figure 32: Boundaries involved in rostrocaudal patterning [42].

As a side note, in contrast to the brain, the spinal cord is patterned by signals from the mesoderm [15].

7.1.2 Canonical WNT Signaling Cascade

Some of the most commonly found signaling proteins are members of the Wnt family. The Wnt pathway developed early in metazoan evolution and has been conserved across many species such as *Drosophila* and humans. The term Wnt was coined as a blend of names of the *Drosophila wingless* gene and the verterbrate homolog *integrated (int-1)*. Wnt signaling has been found to regulate multiple important processes in cell fate specification, cell migration, cell polarity, embryonic organogenesis and of course neural patterning. In humans, 19 different Wnt proteins can be found. All of them

interact with cells by binding to the N-terminal domain of a Frizzled (Fz) receptor protein (and possible co-receptors, such as LRP5/6) residing in and bridging the cell membrane. Here, the signal is transferred inside the cell to Dishevelled (Dsh or Dvl), a cytoplasmic protein. This can trigger at least three downstream cascades – the *canonical*, the *Planar Cell Polarity* and the *Wnt/Ca*$^{2+}$ signaling pathway. We will focus on canonical Wnt signaling.

Simply put, in canonical Wnt signaling, the presence of Wnt prevents the formation of a destruction complex called the *Axin degradasome* that is usually responsible for the degradation of β-catenin. If β-catenin is allowed to accumulate, it will start to translocate into the cell nucleus where it can act on target genes (see Figure 33).

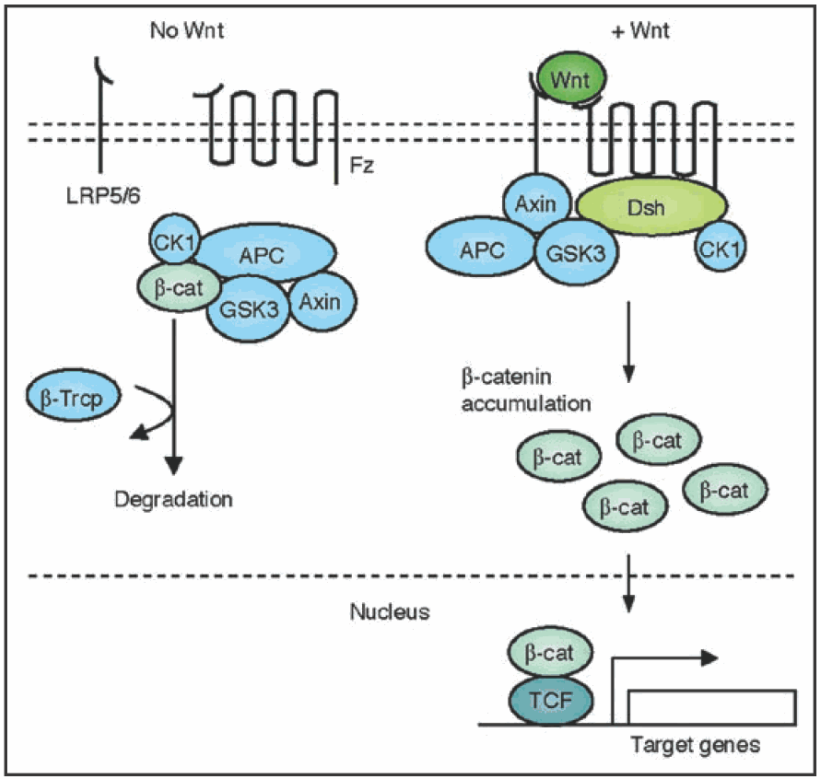

Figure 33: Canonical Wnt Signaling pathway. In the absence of Wnt signals, GSK3, CK1, APC and Axin form a destruction complex that induces the degradation of β-catenin. With Wnt present, the formation of this complex is suppressed and β-catenin can translocate into the cell nucleus, acting on target genes.Taken from [43].

The destruction complex which forms in the absence of a Wnt signal comprises mainly of the scaffold protein Axin, the tumour suppressor adenomatosis polyposis coli (APC) and the two kinases glycogen synthase kinase 3 (GSK3) and casein kinase 1α (CK1α) [44]. When Wnt binds to Fz receptors, Dsh is recruited to the receptor complex where it aids clustered Fz and LRP5/6 receptors in formation of a signalosome by dynamic polymerization of one of its domains. This increases Dsh's avidity for

Axin and also opens up a docking site for Axin on the signalosome [45]. Thus, the whole degradasome is tethered to the signalosome. Due to the resulting closeness, the catalytic pocket of GSK3 is occupied, inhibiting GSK3's activity. This also promotes the degradation of Axin, resulting in an accumulation of β-catenin and its translocation into the nucleus [46]. There, it binds to TCF/LEF factors that are tethered to the Wnt target genes, thus the signaling cascade is complete. [43]

7.1.3 SHH Signaling Cascade

Another major canonical regulator of cell proliferation, cell differentiation as well as cell polarity that has been conserved and adapted across many species is the Sonic Hedgehog (SHH) signaling pathway (Figure 34). The *SHH* gene is the human homolog of the *Drosophila* hedgehog (*Hh*) gene. SHH signaling is responsible for guiding many developmental processes in the embryo, including spinal cord and limb bud tissue differentiation as well as mid- and forebrain neuronal differentiation. It is also responsible for cell proliferation in the adult brain [21].
Without any SHH signals (Figure 34 A), translocation of the transmembrane protein Smoothened (Smo) into the primary cilium (a slim and short protuberance of the cell mebrane) of the cell as well as its activity are repressed. With no Smo activity, protein kinase A (PKA) aids the degradation or processing of full-length Gli transcription factors (Gli2 and Gli3) into Gli repressors (GliR). Gli effectors are a family of zinc-finger proteins that occur as repressors as well as activators in the SHH pathway. GliR can then translocate into the cell nucleus and repress SHH target gene expression.
When SHH binds to the transmembrane receptor Patched1 (Ptc1) (Figure 34 B), Smo can translocate into the primary cilium and repress PKA as well as promote Gli activator (GliA) formation. On top of that, PKA repression inhibits the degradation and processing of full length Gli to GliR, so that a majority of Gli will be available in its active form. GliA can then translocate into the nucleus and activate SHH target gene expression – target genes include *Ptc*, *Shh* and *Gli*. SHH signaling is also influenced by other transmembrane proteins, e.g. it is inhibited by Hhip1 and enhanced by Gas1, Cdo and Boc interception [20].

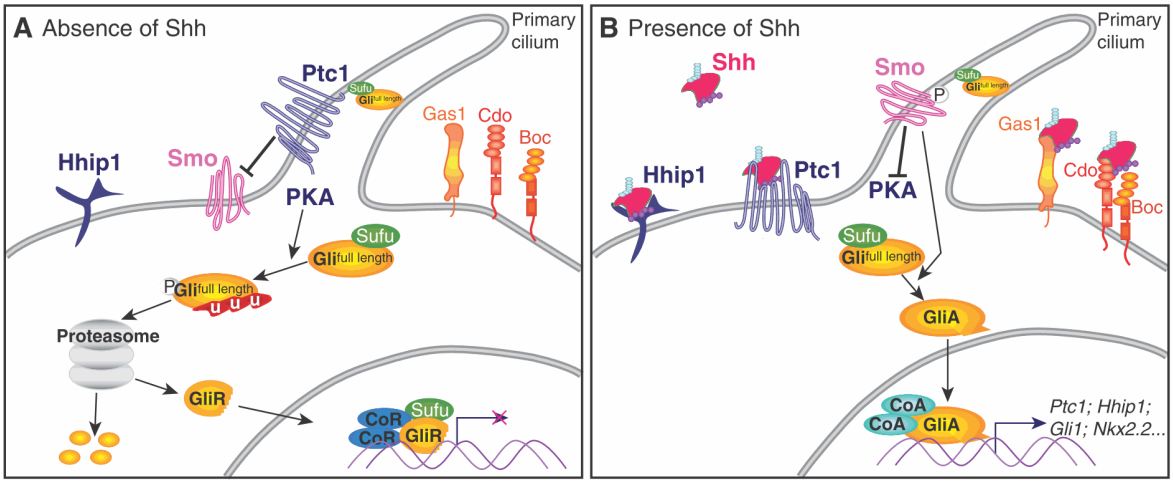

Figure 34: SHH signaling pathway. A: Without any SHH signals, Smo activity is inhibited by Ptc1. Protein kinase A (PKA) is free to aid the processing of Gli transcription factors into repressor form GliR. GliR translocates into the nucleus and represses SHH target genes. B: SHH binds to Ptc1 and Smo represses PKA production. Gli can now be transformed into activator form GliA and promote expression of SHH target genes in the nucleus. Taken from [20].

7.2 Parameters Of Gene Regulatory Networks

Table 1. Parameters of the neural patterning model corresponding to equation 1.

i	1	2	3	4	5	6	7	8	9	10	11	12	13
c_i	0.015	8.00	1000	0.201	0.500	0.201	0.005	0.205	2.00	0.050	0.051	0.248	0.152
n_i	4	4	4	1	2	1	3	1	3	1	3	1	1
δ_i	0.169	0.169	0.170	0.171									

Table 2. Initial gene expression levels of the stochastic simulations on the neural patterning model.

FB	MB	HB	GSK3
1	1	1	1

Figure 35: Parameters for equations 2.1 proposed by Brambach et al. Taken from [28].

Parameters	Description	Value
α	Maximum rate of P	3
β	Maximum rate of O	5
γ	Maximum rate of N	5
h_1	Strength of N repression on P	6
h_2	Strength of O repression on P	2
h_3	Strength of N repression on O	5
h_4	Strength of O repression on N	1
h_5	Strength of P repression on N	1
k_1	Rate of P degradation	1
k_2	Rate of O degradation	1
k_3	Rate of N degradation	1
O_{critP}	Critical value of O for which P value has reached half of its maximal	1
N_{critP}	Critical value of N for which P value has reached half of its maximal	1
O_{critN}	Critical value of O for which N value has reached half of its maximal	1
N_{critO}	Critical value of N for which O value has reached half of its maximal	1
P_{critN}	Critical value of P for which N value has reached half of its maximal	1
n	Hill coefficient of G cooperativity on O	1
m	Hill coefficient of G cooperativity on N	1

Figure 36: Parameters for equations 2.2 proposed by Balaskas et al. Taken from [31].

7.3 Supplementary Figures

7.3.1 Simulation With Test Parameters

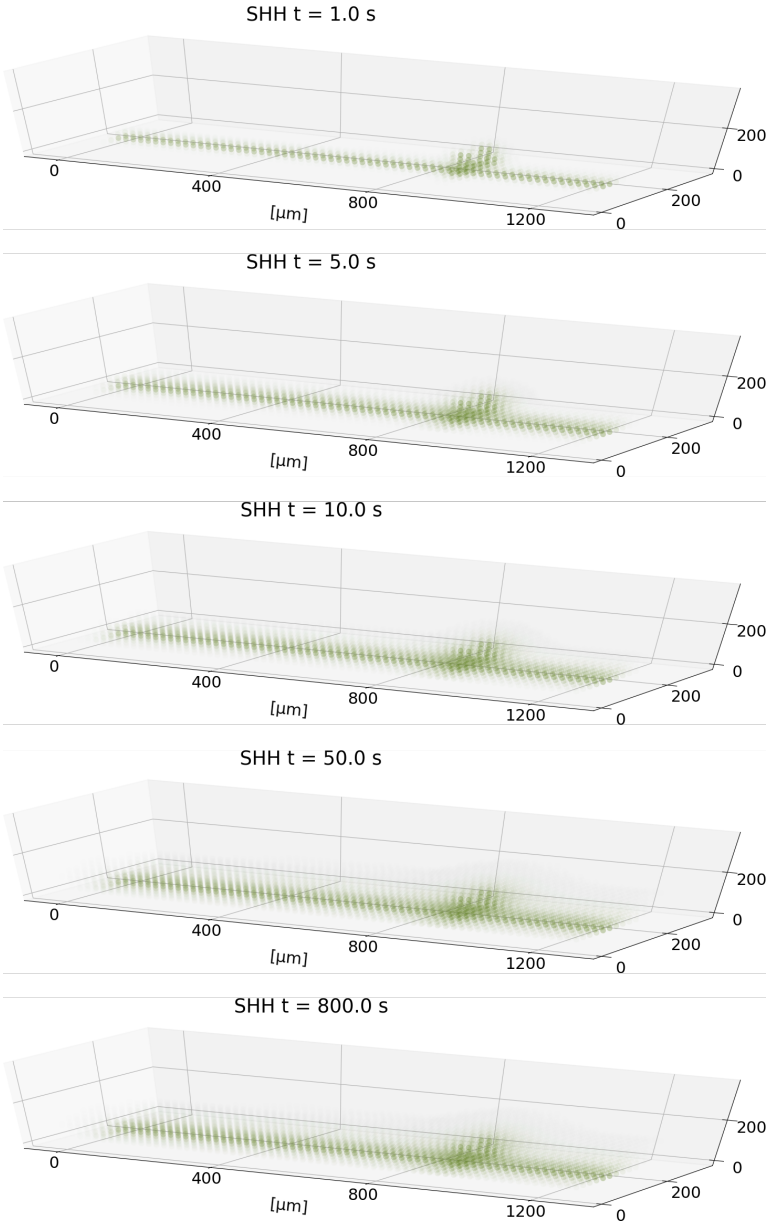

Figure 37: SHH-diffusion for standard parameters. SHH levels are normalized to the level at SHH secretion points.

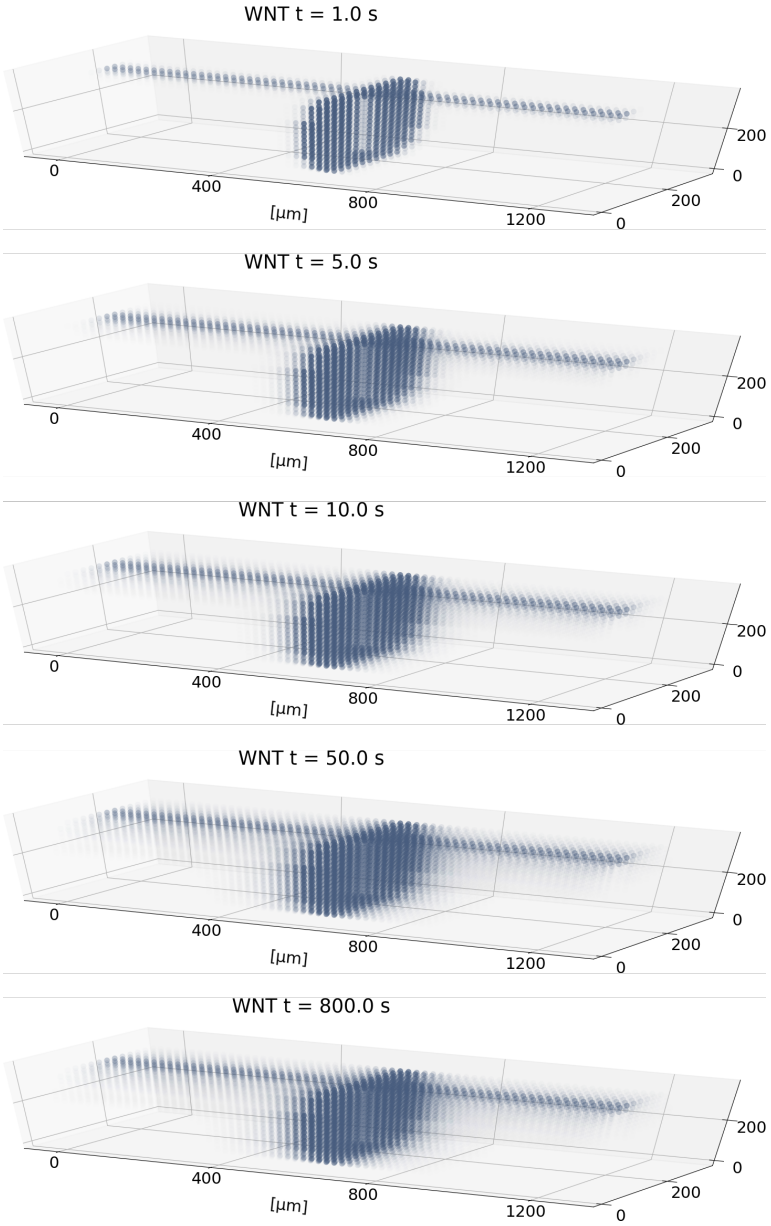

Figure 38: WNT-diffusion for standard parameters. WNT levels are normalized to the level at WNT secretion points.

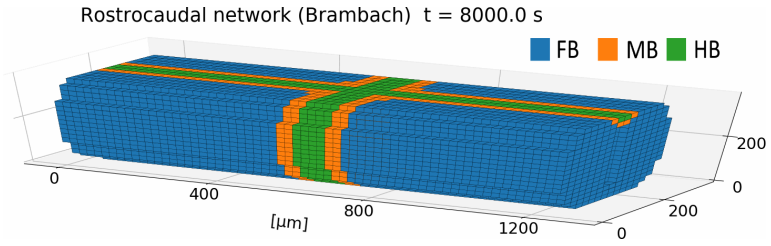

Figure 39: Rostrocaudal patterning at t = 8000.0s.

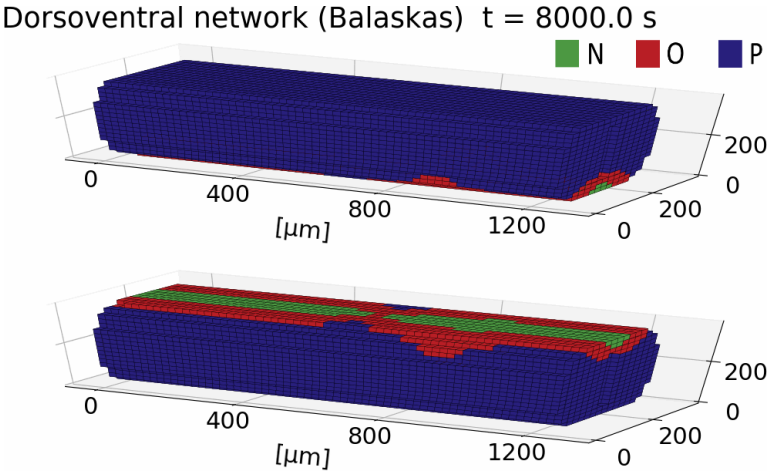

Figure 40: Dorsoventral patterning at t = 8000.0s

7.3.2 WNT-Gli Coupling (W_{critG}, $h6$)

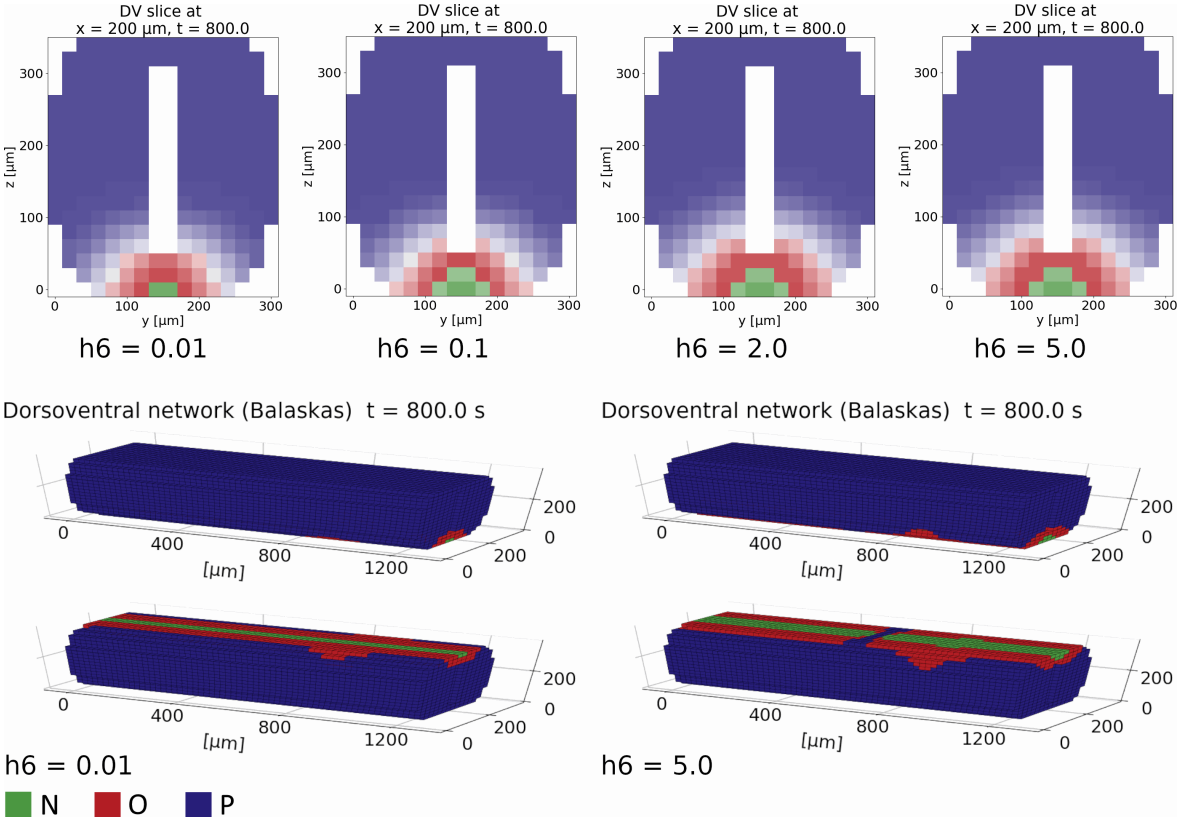

Figure 41: Dorsoventral patterning for varying values of $h6$.

7.3.3 Degradation Rates

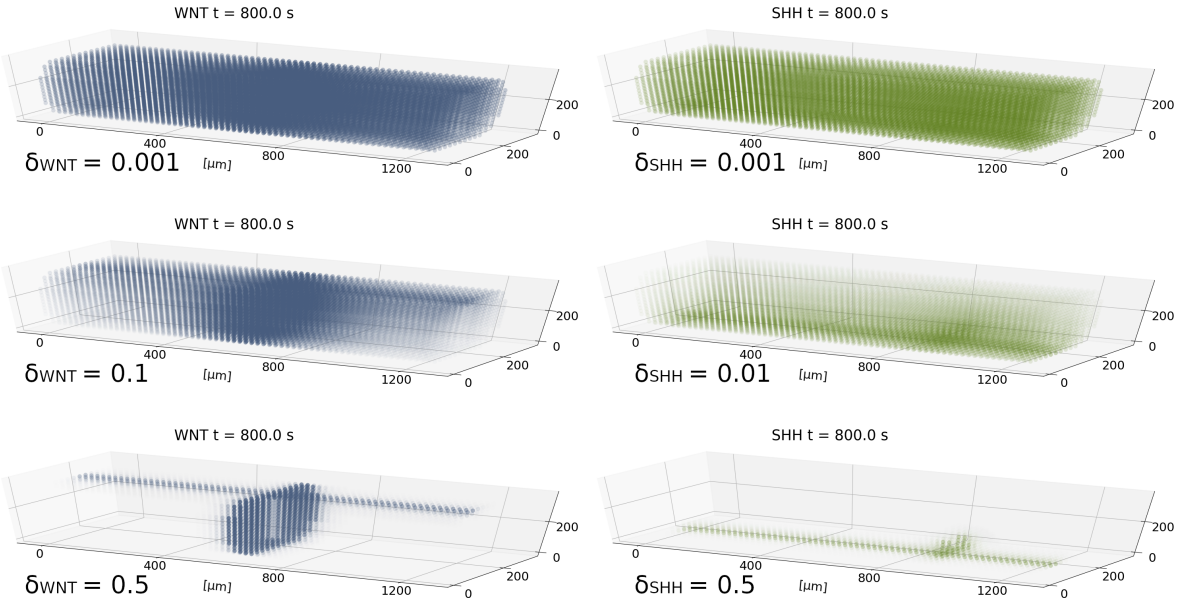

Figure 42: Morphogen levels after 800.0s for varying degradation rates $\delta_{WNT}, \delta_{SHH}$

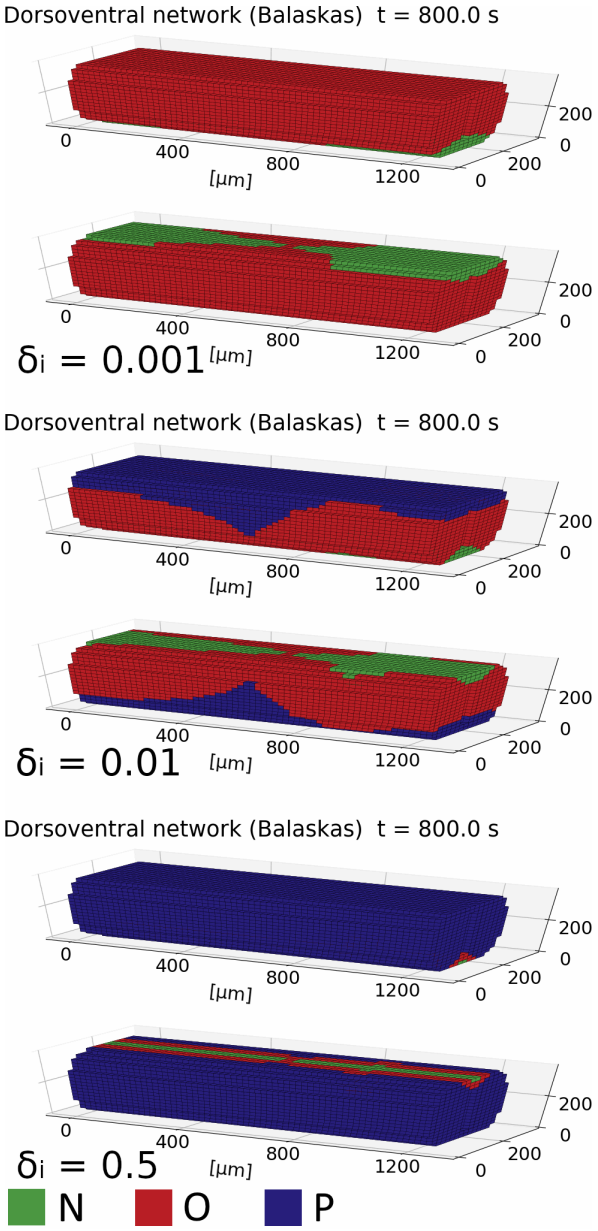

(a) 3d plot

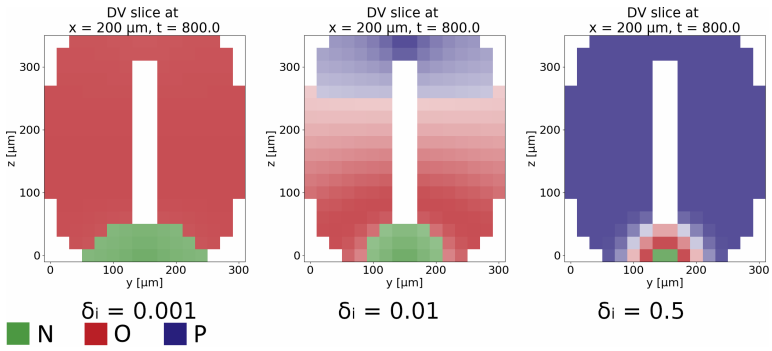

(b) 2d slices

Figure 43: Impact of variation of both degradation rates on rostrocaudal patterning.

References

[1] Eric R Kandel. *Principles of neural science.* New York : McGraw-Hill, 2013 [dvs 2012], 2013. ISBN: 978-0-07-139011-8. JSTOR: LbmcKursbokVefKandel. URL: http://ludwig.lub.lu.se/login?url=http://search.ebscohost.com/login.aspx?direct=true&db=cat07147a&AN=lub.2501561&site=eds-live&scope=site.

[2] Jay B. Bikoff et al. "Spinal Inhibitory Interneuron Diversity Delineates Variant Motor Microcircuits". In: *Cell* 165.1 (Mar. 24, 2016), pp. 207–219. ISSN: 0092-8674. DOI: 10.1016/j.cell.2016.01.027. URL: http://www.sciencedirect.com/science/article/pii/S0092867416300046 (visited on 05/17/2019).

[3] Raffaella Adami, Giuseppe Scesa, and Daniele Bottai. "Stem cell transplantation in neurological diseases: improving effectiveness in animal models". In: *Frontiers in Cell and Developmental Biology* 2 (May 14, 2014). ISSN: 2296-634X. DOI: 10.3389/fcell.2014.00017. URL: https://www.ncbi.nlm.nih.gov/pmc/articles/PMC4206985/ (visited on 05/17/2019).

[4] M. J. Evans and M. H. Kaufman. "Establishment in culture of pluripotential cells from mouse embryos". In: *Nature* 292.5819 (July 9, 1981), pp. 154–156. ISSN: 0028-0836.

[5] Scott F. Gilbert and Michael J. F. Barresi. *Developmental biology.* Sunderland, Massachusetts, U.S.A. : Sinauer Associates, Inc., Publishers, [2016], 2016. ISBN: 978-1-60535-470-5. JSTOR: LbmcKursbokUeGilbert. URL: http://ludwig.lub.lu.se/login?url=http://search.ebscohost.com/login.aspx?direct=true&db=cat07147a&AN=lub.4951647&site=eds-live&scope=site.

[6] Daniela Ferrari et al. "Transplanted dopamine neurons derived from primate ES cells preferentially innervate DARPP-32 striatal progenitors within the graft". In: *The European journal of neuroscience* 24.7 (Oct. 2006), pp. 1885–1896. ISSN: 0953-816X. DOI: 10.1111/j.1460-9568.2006.05093.x. URL: https://www.ncbi.nlm.nih.gov/pmc/articles/PMC2602801/ (visited on 05/17/2019).

[7] Yasushi Takagi et al. "Dopaminergic neurons generated from monkey embryonic stem cells function in a Parkinson primate model". In: *Journal of Clinical Investigation* 115.1 (Jan. 3, 2005), pp. 102–109. ISSN: 0021-9738. DOI: 10.1172/JCI200521137. URL: https://www.ncbi.nlm.nih.gov/pmc/articles/PMC539189/ (visited on 05/17/2019).

[8] Agnete Kirkeby et al. “Generation of Regionally Specified Neural Progenitors and Functional Neurons from Human Embryonic Stem Cells under Defined Conditions”. In: *Cell Reports* 1.6 (June 28, 2012), pp. 703–714. ISSN: 2211-1247. DOI: 10.1016/j.celrep.2012.04.009. URL: https://www.cell.com/cell-reports/abstract/S2211-1247(12)00122-2 (visited on 11/01/2018).

[9] Daniela Lehnen et al. “IAP-Based Cell Sorting Results in Homogeneous Transplantable Dopaminergic Precursor Cells Derived from Human Pluripotent Stem Cells”. In: *Stem Cell Reports* 9.4 (2017), pp. 1207–1220. ISSN: 2213-6711. DOI: 10.1016/j.stemcr.2017.08.016.

[10] *File:Stage11 sem13.jpg - Embryology*. URL: https://embryology.med.unsw.edu.au/embryology/index.php/File:Stage11_sem13.jpg (visited on 05/18/2019).

[11] Amsterdam Academic Medical Center (AMC). *3datlas*. 3D Atlas of Human Embryology. URL: https://www.3dembryoatlas.com/ (visited on 02/07/2019).

[12] M.A. Hill. *Embryology Main Page*. In: *UNSW Embryology*. ISBN: 978 0 7334 2609 4. URL: https://embryology.med.unsw.edu.au/embryology/index.php/Main_Page.

[13] Ronan R. O’Rahilly and Fabiola Müller. *The Embryonic Human Brain: An Atlas Of Developmental Stages*. John Wiley & Sons, Sept. 18, 2006. 375 pp. ISBN: 978-0-471-97307-2.

[14] *HGNC Guidelines — HUGO Gene Nomenclature Committee*. URL: https://www.genenames.org/about/guidelines/#!/#tocAnchor-1-18 (visited on 02/14/2019).

[15] Larry R. Squire. *Fundamental neuroscience*. 3rd ed. Amsterdam : Elsevier, cop. 2008, 2008. ISBN: 978-0-12-374019-9. JSTOR: LmelKursbokVef{FUNDAMENTAL}. URL: http://ludwig.lub.lu.se/login?url=http://search.ebscohost.com/login.aspx?direct=true&db=cat07147a&AN=lub.1762101&site=eds-live&scope=site.

[16] Simon LeVay, Janice Baldwin, and John Baldwin. *Discovering Human Sexuality*. Google-Books-ID: LVWctAEACAAJ. Oxford University Press, 2018. 696 pp. ISBN: 978-1-60535-669-3.

[17] Mina Gouti, Vicki Metzis, and James Briscoe. “The route to spinal cord cell types: a tale of signals and switches”. In: *Trends in Genetics* 31.6 (June 1, 2015), pp. 282–289. ISSN: 0168-9525. DOI: 10.1016/j.tig.2015.03.001. URL: http://

www.sciencedirect.com/science/article/pii/S0168952515000396 (visited on 04/29/2019).

[18] U. F. O. Themes. *Nervous System Organization and Development*. Basicmedical Key. June 16, 2017. URL: https://basicmedicalkey.com/nervous-system-organization-and-development/ (visited on 04/28/2019).

[19] Daniel Marbach, Claudio Mattiussi, and Dario Floreano. "Bio-mimetic Evolutionary Reverse Engineering of Genetic Regulatory Networks". In: *Evolutionary Computation,Machine Learning and Data Mining in Bioinformatics*. Ed. by Elena Marchiori, Jason H. Moore, and Jagath C. Rajapakse. Lecture Notes in Computer Science. Springer Berlin Heidelberg, 2007, pp. 155–165. ISBN: 978-3-540-71783-6.

[20] Vanessa Ribes and James Briscoe. "Establishing and Interpreting Graded Sonic Hedgehog Signaling during Vertebrate Neural Tube Patterning: The Role of Negative Feedback". In: *Cold Spring Harbor Perspectives in Biology* (July 15, 2009), a002014. ISSN: , 1943-0264. DOI: 10.1101/cshperspect.a002014. URL: http://cshperspectives.cshlp.org/content/early/2009/07/13/cshperspect.a002014 (visited on 11/19/2018).

[21] Karen Lai, Matthew J. Robertson, and David V. Schaffer. "The Sonic Hedgehog Signaling System as a Bistable Genetic Switch". In: *Biophysical Journal* 86.5 (May 1, 2004), pp. 2748–2757. ISSN: 0006-3495. DOI: 10.1016/S0006-3495(04)74328-3. URL: http://www.sciencedirect.com/science/article/pii/S0006349504743283 (visited on 02/14/2019).

[22] Ulrika Nordström, Thomas M. Jessell, and Thomas Edlund. "Progressive induction of caudal neural character by graded Wnt signaling". In: *Nature Neuroscience* 5.6 (June 2002), pp. 525–532. ISSN: 1097-6256. DOI: 10.1038/nn854.

[23] Bruce M Carlson. *Human embryology and developmental biology*. OCLC: 253216824. Edinburgh: Mosby, 2008. ISBN: 978-0-323-05385-3.

[24] Holly C. Gibbs et al. "Midbrain-Hindbrain Boundary Morphogenesis: At the Intersection of Wnt and Fgf Signaling". In: *Frontiers in Neuroanatomy* 11 (2017). ISSN: 1662-5129. DOI: 10.3389/fnana.2017.00064. URL: https://www.frontiersin.org/articles/10.3389/fnana.2017.00064/full (visited on 04/29/2019).

[25] Anselme L. Perrier et al. “Derivation of midbrain dopamine neurons from human embryonic stem cells”. In: *Proceedings of the National Academy of Sciences* 101.34 (Aug. 24, 2004), pp. 12543–12548. ISSN: 0027-8424, 1091-6490. DOI: 10.1073/pnas.0404700101. URL: https://www.pnas.org/content/101/34/12543 (visited on 04/30/2019).

[26] Yiping Yan et al. “Directed Differentiation of Dopaminergic Neuronal Subtypes from Human Embryonic Stem Cells”. In: *STEM CELLS* 23.6 (2005), pp. 781–790. ISSN: 1549-4918. DOI: 10.1634/stemcells.2004-0365. URL: https://stemcellsjournals.onlinelibrary.wiley.com/doi/abs/10.1634/stemcells.2004-0365 (visited on 04/30/2019).

[27] Yunlong Tao and Su-Chun Zhang. “Neural Subtype Specification from Human Pluripotent Stem Cells”. In: *Cell Stem Cell* 19.5 (Nov. 3, 2016), pp. 573–586. ISSN: 1934-5909. DOI: 10.1016/j.stem.2016.10.015. URL: http://www.sciencedirect.com/science/article/pii/S1934590916303551 (visited on 04/29/2019).

[28] Max Brambach. *From naive pluripotent stem cells to neuron progenitors A study of the central gene regulatory networks in human. Master Thesis. Lund University.* June 2018.

[29] Fausto Ulloa and Elisa Martí. “Wnt won the war: Antagonistic role of Wnt over Shh controls dorso-ventral patterning of the vertebrate neural tube”. In: *Developmental Dynamics* 239.1 (Jan. 1, 2010), pp. 69–76. ISSN: 1097-0177. DOI: 10.1002/dvdy.22058. URL: https://onlinelibrary.wiley.com/doi/abs/10.1002/dvdy.22058 (visited on 11/01/2018).

[30] Leigh Wilson and Malcolm Maden. “The mechanisms of dorsoventral patterning in the vertebrate neural tube”. In: *Developmental Biology* 282.1 (June 1, 2005), pp. 1–13. ISSN: 0012-1606. DOI: 10.1016/j.ydbio.2005.02.027. URL: http://www.sciencedirect.com/science/article/pii/S001216060500134X (visited on 05/19/2019).

[31] Nikolaos Balaskas et al. “Gene Regulatory Logic for Reading the Sonic Hedgehog Signaling Gradient in the Vertebrate Neural Tube”. In: *Cell* 148.1 (Jan. 20, 2012), pp. 273–284. ISSN: 0092-8674. DOI: 10.1016/j.cell.2011.10.047. URL: http://www.sciencedirect.com/science/article/pii/S0092867411013602 (visited on 09/10/2018).

[32] Dianqing Wu and Weijun Pan. "GSK3: a multifaceted kinase in Wnt signaling". In: *Trends in biochemical sciences* 35.3 (Mar. 2010), pp. 161–168. ISSN: 0968-0004. DOI: 10.1016/j.tibs.2009.10.002. URL: https://www.ncbi.nlm.nih.gov/pmc/articles/PMC2834833/ (visited on 01/21/2019).

[33] @ephtracy. *MagicaVoxel*. URL: https://ephtracy.github.io/ (visited on 05/15/2019).

[34] Benjamin A. Stickler and Ewald Schachinger. *Basic Concepts in Computational Physics*. 2nd ed. Springer International Publishing, 2016. ISBN: 978-3-319-27263-4. URL: https://www.springer.com/de/book/9783319272634 (visited on 04/01/2019).

[35] Charles Hirsch, ed. *Numerical Computation of Internal & External Flows: Fundamentals of Numerical Discretization*. New York, NY, USA: John Wiley & Sons, Inc., 1988. ISBN: 978-0-471-91762-5.

[36] Opiyo Richard Otieno et al. "Finite Difference Analysis of 2-Dimensional Acoustic Wave with a Signal Function". In: 6.10 (2015), p. 14.

[37] William H. Press et al. *Numerical Recipes in C (2Nd Ed.): The Art of Scientific Computing*. New York, NY, USA: Cambridge University Press, 1992. ISBN: 978-0-521-43108-8.

[38] Liu Hong and Jinzhi Lei. "Scaling law for the radius of gyration of proteins and its dependence on hydrophobicity". In: *Journal of Polymer Science Part B: Polymer Physics* 47.2 (Jan. 15, 2009), pp. 207–214. ISSN: 1099-0488. DOI: 10.1002/polb.21634. URL: https://onlinelibrary.wiley.com/doi/abs/10.1002/polb.21634 (visited on 11/08/2018).

[39] *WNT1 - Protein Wnt - Pan troglodytes (Chimpanzee) - WNT1 gene & protein*. URL: https://www.uniprot.org/uniprot/A0A2J8LQ70 (visited on 05/07/2019).

[40] https://www.uniprot.org/uniprot/Q15465. *SHH - Sonic hedgehog protein precursor - Homo sapiens (Human) - SHH gene & protein*. URL: https://www.uniprot.org/uniprot/Q15465 (visited on 11/08/2018).

[41] Lizhong He and Bernd Niemeyer. "A Novel Correlation for Protein Diffusion Coefficients Based on Molecular Weight and Radius of Gyration". In: *Biotechnology Progress* 19.2 (Jan. 1, 2003), pp. 544–548. ISSN: 1520-6033. DOI: 10.1021/bp0256059. URL: https://onlinelibrary.wiley.com/doi/abs/10.1021/bp0256059 (visited on 11/08/2018).

[42] Clemens Kiecker and Andrew Lumsden. "Compartments and their boundaries in vertebrate brain development". In: *Nature Reviews Neuroscience* 6.7 (July 2005), pp. 553–564. ISSN: 1471-0048. DOI: 10.1038/nrn1702. URL: http://www.nature.com/articles/nrn1702 (visited on 04/28/2019).

[43] Yuko Komiya and Raymond Habas. "Wnt signal transduction pathways". In: *Organogenesis* 4.2 (2008), pp. 68–75. ISSN: 1547-6278. URL: https://www.ncbi.nlm.nih.gov/pmc/articles/PMC2634250/ (visited on 02/12/2019).

[44] Melissa Gammons and Mariann Bienz. "Multiprotein complexes governing Wnt signal transduction". In: *Current Opinion in Cell Biology*. Cell Signalling 51 (Apr. 1, 2018), pp. 42–49. ISSN: 0955-0674. DOI: 10.1016/j.ceb.2017.10.008. URL: http://www.sciencedirect.com/science/article/pii/S0955067417300418 (visited on 02/13/2019).

[45] Chan Gao and Ye-Guang Chen. "Dishevelled: The hub of Wnt signaling". In: *Cellular Signalling* 22.5 (May 1, 2010), pp. 717–727. ISSN: 0898-6568. DOI: 10.1016/j.cellsig.2009.11.021. URL: http://www.sciencedirect.com/science/article/pii/S0898656809003684 (visited on 02/13/2019).

[46] Adam Cliffe, Fumihiko Hamada, and Mariann Bienz. "A Role of Dishevelled in Relocating Axin to the Plasma Membrane during Wingless Signaling". In: *Current Biology* 13.11 (May 27, 2003), pp. 960–966. ISSN: 0960-9822. DOI: 10.1016/S0960-9822(03)00370-1. URL: http://www.sciencedirect.com/science/article/pii/S0960982203003701 (visited on 02/13/2019).